Two decades of permafrost region CO_2, CH4, and N2O budgets suggest a small net greenhouse gas source to the atmosphere

Submitted for review with Global Biogeochemical Cycles, within the RECCAP2 special issue

Hugelius G., Ramage J., Burke E, Chatterjee A., Smallman T. L., Aalto T., Bastos A., Biasi C., Canadell J.G., Chandra N., Chevallier F., Ciais P., Chang J., Feng L., Jones M.W., Kleinen T., Kuhn M., Lauerwald R., Liu J., López-Blanco E., Luijkx I.T., Marushchak M.E., Natali S.M., Niwa Y., Olefeldt D., Palmer P. I., Patra P.K., Peters W., Potter S., Poulter B., Rogers B. M., Riley W.J., Saunois M., Schuur E.A.G., Thompson R., Treat C., Tsuruta A., Turetsky M.R., Virkkala A.-M., Voigt C., Watts J., Zhu Q. and Zheng B.*

Corresponding author*: gustaf.hugelius@natgeo.su.se, ORCID 0000-0002-8096-1594

Affiliations

Hugelius, Gustaf and Ramage, Justine: Department of Physical Geography and Bolin Centre for Climate Research, Stockholm University, SE10691, Sweden.

Burke, Eleanor: Met Office Hadley Centre, FitzRoy Road, Exeter, EX1 3PB, UK

Chatterjee, Abhishek and Liu J.: Jet Propulsion Laboratory, California Institute of Technology, Pasadena, CA 91109, USA

Smallman T. Luke: School of GeoSciences and National Centre for Earth Observation, University of Edinburgh, Edinburgh, EH9 3FF, UK

Aalto Tuula. and Tsuruta Aki. Finnish Meteorological Institute, Helsinki, Finland

Bastos, Ana: Max Planck Institute for Biogeochemistry, Dept. of Biogeochemical Integration, 07745 Jena, Germany

Biasi, Christina: University of Eastern Finland, Department of Environmental and Biological Sciences, Yliopistonranta 1 E, 70210 Kuopio, Finland and University of Innsbruck, Department of Ecology, Sternwartstrasse 15, 6020 Innsbruck, Austria

Canadell, Josep G.: Global Carbon Project, CSIRO Environment, Canberra, ACT 2601, Australia

Chandra, Patra: Research Institute for Global Change, JAMSTEC, Yokohama, 2360001, Japan

Chevallier F., Ciais P. and Saunois M. : Laboratoire des Sciences du Climat et de l'Environnement, LSCE-IPSL (CEA-CNRS-UVSQ), Université Paris-Saclay 91191 Gif-sur-Yvette, France

Chang J.: College of Environmental and Resource Sciences, Zhejiang University, 310058, Hangzhou, China

Feng L. and P. I. Palmer, National Center for Earth Observation, University of Edinburgh, Edinburgh, UK

Jones, Matthew W.: Tyndall Centre for Climate Change Research, School of Environmental Sciences, University of East Anglia (UEA), Norwich, NR4 7TJ, UK

Kleinen, Thomas: Max Planck Institute for Meteorology, Bundesstr. 53, 20146 Hamburg, Germany

Kuhn, Mckenize: Department of Earth Sciences. University of New Hampshire. Durham, NH 03824,USA

Lauerwald, R.: Université Paris-Saclay, INRAE, AgroParisTech, UMR Ecosys, 91120 Palaiseau, France.

López-Blanco, Efrén: Department of Ecoscience, Arctic Research Center, Aarhus University, Frederiksborgvej 399, 4000 Roskilde, Denmark (double affiliation) and Department of Environment and Minerals, Greenland Institute of Natural Resources, PO box 570, 3900 Nuuk, Greenland

Luijkx, I.T. and Peters W: Meteorology and Air Quality Group, Wageningen University, P.O. Box 47, 6700 AA Wageningen, the Netherlands

Marushchak M.E, Voigt, C.: University of Eastern Finland, Department of Environmental and Biological Sciences, Yliopistonranta 1 E, 70210 Kuopio, Finland

Rogers Brendan, Anna Virkkala, Stefano Potter, Sue Natali, Jennifer Watts: Woodwell Climate Research Center, 149 Woods Hole Road, Falmouth, MA, USA

Niwa, Yosuke: Earth System Division, National Institute for Environmental Studies, Tsukuba, Japan (double affiliation) and Yosuke Niwa: Department of Climate and Geochemistry Research, Meteorological Research Institute, Tsukuba, Japan

Olefeldt, David: Department of Renewable Resources, University of Alberta, Edmonton, Alberta, Canada

Patra P.: Research Institute for Humanity and Research, Kyoto, 603 8047, Japan

Peters, W.: (double) University of Groningen, Centre for Isotope Research, 9747 AG Groningen The Netherlands

Poulter, Benjamin: NASA GSFC, Biospheric Sciences Lab., Greenbelt, MD 20771, USA

Riley W.J and Zhu, Q: Climate and Ecosystem Sciences Division, Lawrence Berkeley National Laboratory, Berkeley, CA 94720, USA

Schuur EAG Center for Ecosystem Science and Society, and Department of Biological Sciences, Northern Arizona University, Flagstaff, AZ 86001 USA

Thompson, Rona L.: Norsk Institutt for Luftforskning, NILU, Kjeller, Norway

Treat Claire: Alfred Wegener Institute Helmholtz Center for Polar and Marine Research, 14473 Potsdam, Germany

Turetsky, Merrit: Institute of Arctic and Alpine Research and Department of Ecology and Evolutionary Biology, University of Colorado, Boulder CO USA

Voigt, C.: Institute of Soil Science, University of Hamburg, 20146 Hamburg, Germany

Zheng B.: Shenzhen Key Laboratory of Ecological Remediation and Carbon Sequestration, Institute of Environment and Ecology, Tsinghua Shenzhen International Graduate School, Tsinghua University, Shenzhen 518055, China.

Abstract

The long-term net sink of carbon (C), nitrogen (N) and greenhouse gases (GHGs) in the northern permafrost region is projected to weaken or shift under climate change. But large uncertainties remain, even on present-day GHG budgets. We compare bottom-up (data-driven upscaling, process-based models) and top-down budgets (atmospheric inversion models) of the main GHGs (CO_2, CH_4, and N_2O) and lateral fluxes of C and N across the region over 2000-2020. Bottom-up approaches estimate higher land to atmosphere fluxes for all GHGs compared to top-down atmospheric inversions. Both bottom-up and top-down approaches respectively show a net sink of CO_2 in natural ecosystems (-31 (-667, 559) and -587 (-862, -312), respectively) but sources of CH4 (38 (23, 53) and 15 (11, 18) Tg CH4-C yr-1) and N2O (0.6 (0.03, 1.2) and 0.09 (-0.19, 0.37) Tg N2O-N yr-1) in natural ecosystems. Assuming equal weight to bottom-up and top-down budgets and including anthropogenic emissions, the combined GHG budget is a source of 147 (-492, 759) Tg CO_2-Ceq yr-1 (GWP100). A net CO_2 sink in boreal forests and wetlands is offset by CO_2 emissions from inland waters and CH_4 emissions from wetlands and inland waters, with a smaller additional warming from N_2O emissions. Priorities for future research include representation of inland waters in process-based models and compilation of process-model ensembles for CH_4 and N_2O. Discrepancies between bottom-up and top-down methods call for analyses of how prior flux ensembles impact inversion budgets, more in-situ flux observations and improved resolution in upscaling.

Introduction

The northern permafrost region covers 22% of the northern hemisphere land mass, is dominated by taiga and tundra ecosystems, and is an important component in the global cycles of carbon (C) and nitrogen (N) (Obu et al., 2019; Schuur et al., 2022). The permafrost region warms at rates 2-4 times faster than the global average and climate-driven changes in the extent and temperature of permafrost have been observed (Biskaborn et al., 2019; Rantanen et al., 2022). As soils become warmer or thaw, increased microbial decomposition of soil organic matter (SOM) is projected to cause net losses of C and N to the atmosphere or to aquatic ecosystems (Schuur et al., 2022). Climate change and permafrost thaw also affect and interact with other ecosystem properties, including vegetation dynamics, different disturbance regimes, and the distribution and flow of water through the landscape (Treharne et al., 2022). All of these factors affect the seasonal and annual budgets of the important greenhouse gases (GHGs) carbon dioxide (CO_2), methane (CH_4), and nitrous oxide (N_2O) as well as downstream lateral fluxes of C and N.

Permafrost is ground that is at or below 0°C for at least two consecutive years and underlies circa 14 million km^2 of land in the Northern Hemisphere (Obu, 2021). The northern permafrost region by definition also includes areas with spatially discontinuous permafrost coverage, and covers circa 22 million km^2 of land when permafrost-free areas within the region are included (Obu, 2021). Warming of the active layer and permafrost, gradual thaw and abrupt thaw are occurring across the permafrost domain (Nitze et al., 2018; Runge et al., 2022; Smith et al., 2022) and may increase decomposition of SOM, rich in both C and N, which has accumulated over millenia under cold and wet conditions. Permafrost region soils are estimated to store 1000±200 Pg of organic C and 60±20 Pg of N in the upper three metres (Hugelius et al., 2014; Mishra et al., 2021; Palmtag et al., 2022). Of the total C storage, about 330±80 Pg C is stored in peatlands (Hugelius et al., 2014, 2020), and the rest in mineral soil, often enriched in C by repeated deposition or frost heave processes (Tarnocai et al., 2009). Deeper unconsolidated sedimentary deposits store an additional 400-1000 Pg C, making the permafrost region the largest terrestrial C and N pool on Earth (Strauss et al., 2021).

As soils thaw or become warmer, enhanced microbial processing of soil C and N causes release of GHGs (CO_2, CH_4 and N_2O) into the atmosphere which cause further warming and forming a positive feedback loop known as the "permafrost carbon feedback" (Schuur et al., 2008, 2022). Hereafter we refer to it as the "permafrost GHG feedback", to include non-carbon feedbacks, such as from N_2O. The sixth assessment report of the Intergovernmental Panel on Climate Change (IPCC) (Canadell et al. 2021) estimated that the permafrost GHG feedback from CO_2 per degree of global warming at the end of the century is 18 (3.1 to 41, 5–95% range) PgC $°C^{-1}$, with an additional permafrost GHG

143 feedback from CH_4 of 2.8 (0.7 to 7.3) PgCeq $°C^{-1}$. However, this IPCC estimate does not fully include
144 abrupt permafrost thaw processes which cause strong additional release of CO_2 and CH_4 at decadal to
145 centennial time scales, especially from release of CH_4 from water-logged post-thaw environments
146 (Turetsky et al., 2020). Abrupt thaw, including thaw-lake formation, collapse of permafrost peatlands,
147 and thaw-slump formation, can rapidly affect permafrost at depths of several metres, causing rapid
148 melting of ground ice, land subsidence and a complete restructuring of the landscape. In addition to
149 uncertainties in how climate warming drives increased respiration, there is large uncertainty
150 regarding mediating effects from increased vegetation productivity (and CO_2 uptake) caused by longer
151 growing seasons, increased CO_2 concentrations, and additional nutrient release from thawing
152 permafrost (Abbott et al., 2016; Liu et al., 2022; McGuire et al., 2018). While uncertainties remain
153 large, many studies based on observational GHG flux time series show enhanced net GHG emissions
154 from warming and thawing permafrost soils (Kuhn et al., 2021; Marushchak et al., 2021; Natali et al.,
155 2015; Rodenhizer et al., 2022; Voigt et al., 2017, 2019).
156
157 A potential shift from a net GHG sink to a source remains uncertain in projections using Earth System
158 models (ESMs). A recent study using the CMIP6 ensemble of ESMs projects a sustained northern
159 CO_2 sink from 2015-2100 across a broad range of human emissions scenarios (Qiu et al., 2023).
160 However, the majority of the CMIP6 models do not include an explicit representation of permafrost,
161 or GHG feedbacks from thaw, and are thus likely unable to properly project changes in permafrost
162 GHG balance under future warming. A previous intercomparison of process-models with
163 representation of gradual permafrost thaw found that the northern permafrost region would act as a
164 sustained net C sink under medium emission scenarios (RCP4.5), but would likely act as a C source
165 under higher emissions scenarios, at least over the long term (McGuire et al., 2018). However, there
166 was significant spread between different models, largely reflecting limited representation of processes
167 affecting vegetation productivity, soil respiration and permafrost dynamics. There is also mounting
168 evidence that other localized disturbance processes, still lacking in global models, play an important
169 role in the mobilization of permafrost C and N. This includes disturbances associated with abrupt
170 thaw, coastal erosion, fires, pests or windfalls (Foster et al., 2022; Holloway et al., 2020; Hugelius et
171 al., 2020; Marushchak et al., 2021; Walker et al., 2019). While progress is continuously being made,
172 model simulations of the interactions between permafrost and disturbances are in their infancy
173 (Treharne et al., 2022) and are often only relevant for specific field sites (Aas et al., 2019; Brown et
174 al., 2015; López-Blanco et al., 2022). Similarly, the lateral export of C in the form of dissolved
175 organic C (DOC) is missing in most ESMs. Moreover, dedicated simulations of permafrost region
176 N_2O fluxes are still scarce and process information is insufficiently available (Lacroix et al., 2022;
177 Voigt et al., 2020).
178

Improved understanding of GHG exchange in the permafrost region is therefore crucial for constraining global GHG budget estimates and reducing discrepancies between methods (Friedlingstein et al., 2022; Saunois et al., 2020; Tian et al., 2020). Estimates of GHG budgets are typically done using bottom-up (data-driven ecosystem flux upscaling - hereafter referred to as ecosystem flux upscaling - or process-based models) or top-down (from inversions of atmospheric GHG mole fractions - hereafter referred to as atmospheric inversion models) approaches (Ciais et al., 2022). Budgets based on ecosystem flux upscaling combine observations of GHG fluxes with geospatial datasets, while process-based model budgets are based on mathematical representations of ecosystem processes characterizing the functioning of biogeophysical systems. Here, we also compare the other bottom-up approaches to a terrestrial model-data fusion (MDF) approach, where a process-model is calibrated at pixel-scale using a Bayesian algorithm and spatially coherent observations interpolated from field data and satellite-based Earth Observation (EO). Atmospheric inversion models use advanced mathematical methods to estimate surface-to-atmosphere net GHG fluxes by combining atmospheric GHG concentration information (in-situ or flask measurements from surface stations, or total column abundances estimated from satellites), gridded prior flux information, and atmospheric transport models. The first comprehensive GHG budget synthesizing bottom-up and top-down GHG estimates for the Arctic tundra was published in 2012 as part of the REgional Carbon Cycle Assessment and Processes project (RECCAP, McGuire et al., 2012) and highlighted the high variability between budgeting methods thus calling for more efforts to identify and reduce the sources of discrepancies. Although much progress has been made in the decade that followed, some of these issues remain unresolved and there has been no systematic review of GHG budgets for the full permafrost region (including boreal and tundra biomes) that compares and reconciles different budgeting approaches (bottom-up and top-down).

Here we present comprehensive budgets of GHGs (CO_2, CH_4, and N_2O) and lateral fluxes of C and N for the period 2000-2020 across the northern permafrost region. We compare estimated GHG fluxes from the permafrost region using bottom-up and top-down approaches and identify remaining research gaps that must be addressed in order to reconcile the different budget estimates and improve interpretations of GHG budgets. The budgets also include estimated anthropogenic emissions of CO_2 and CH_4. These permafrost regional budgets are part of the REgional Carbon Cycle Assessment and Processes-2 (RECCAP2) project of the Global Carbon Project that aims to collect and integrate regional GHGs budgets covering all global lands and oceans (Ciais et al., 2022) (https://www.globalcarbonproject.org/reccap/).

Methods

Study area

The spatial extent of permafrost defined in this study includes areas within the northern permafrost region as defined in Obu et al. (2021) and restricted to the Boreal Arctic Wetlands and Lakes Dataset area (BAWLD), (Olefeldt et al., 2021) (Fig 1). This restriction was made due to constraints in data availability for ecosystem flux upscaling. As a consequence the targeted BAWLD-RECCAP2 permafrost domain does not take into account areas underlain by permafrost in Central Asia and the Tibetan plateau (blue areas outside the black line in figure 1). The BAWLD-RECCAP2 permafrost region considered in this study is 18.42 million km^2 (excluding ice sheets and glaciers). Because much of the region is underlain by spatially discontinuous permafrost in a mosaic of different land forms and ecosystems, areas and land cover types without permafrost are included to the domain. All flux estimates and models were run or rescaled to 0.5 x 0.5 degree spatial resolution and masked to match the BAWLD-RECCAP2 permafrost region (hereafter permafrost region). We differentiated tundra and boreal forest areas within the permafrost region using a biome delineation (Dinerstein et al., 2017). The study area overlaps several other RECCAP2 regions (Ciais et al., 2022) but no specific effort to harmonize the budgets presented here with the RECCAP2 budgets of those regions are made in this paper.

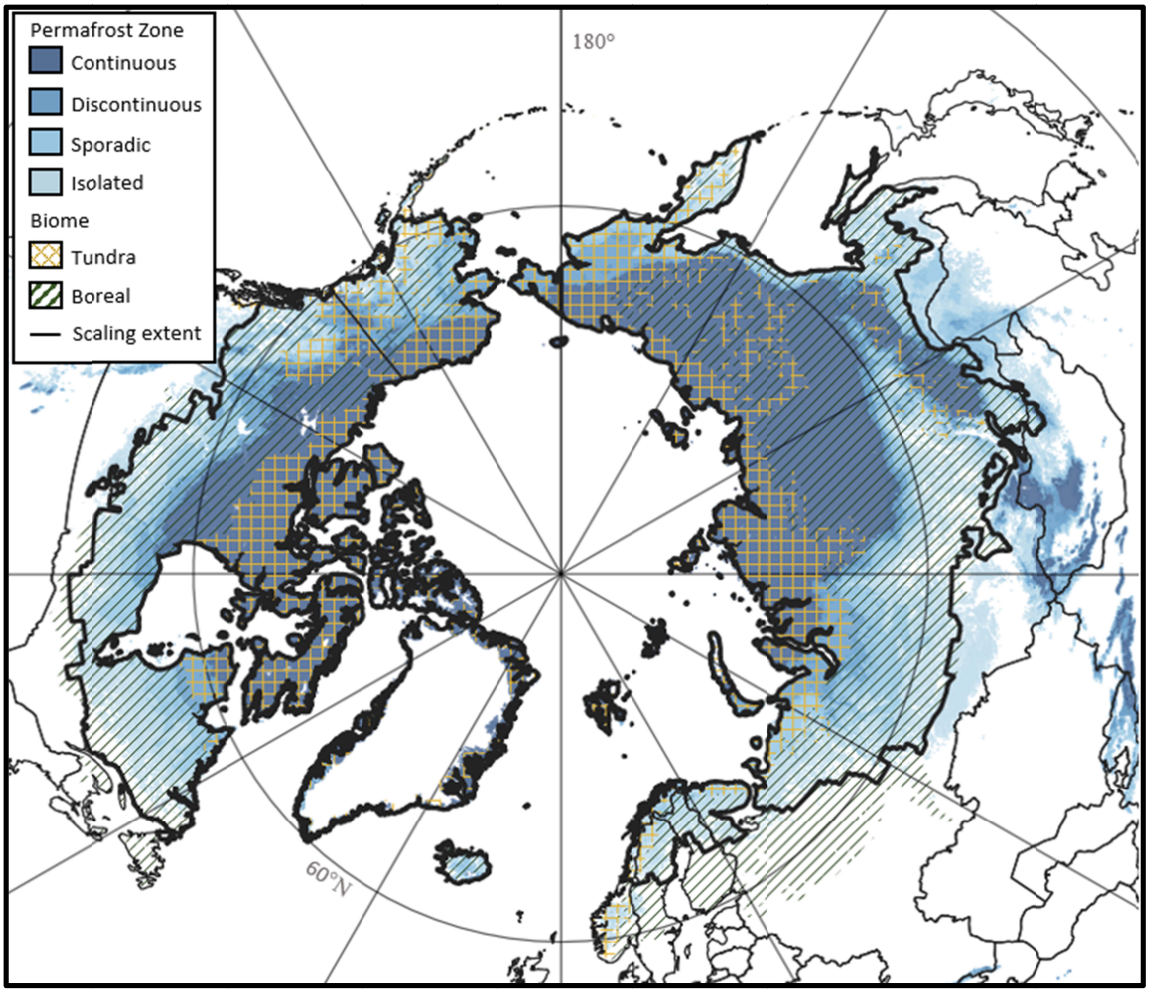

Figure 1: Map of the extent of the study area, defined as were the northern permafrost region (blue shades, data from Obu et al., 2021) overlaps with the spatial extent of the Tundra and Boreal forest biomes (hatched areas) as represented Boreal Arctic Wetlands and Lakes Dataset (BAWLD, Olefeldt et al., 2021). Because the permafrost extent in non-continuous in much of the region, it includes large areas of permafrost-free ecosystems in a mosaic within the broader region. Figure S1 in the supplement shows the additional areas that recorded mean annual air temperature (MAAT) below 0°C between 1990 and 2000 (full extent of ISIMIP3 permafrost model intercomparison), but which were excluded from this budget estimate because they are outside the BAWLD extent.

Summary of overall budget approach

This paper presents full annual budgets of C and N fluxes in the form of the main GHGs (CO_2, CH_4 and N_2O) and as lateral fluxes in streams and rivers and from coastal erosion for the time period 2000-2020. All budgets are expressed on a C and N mass basis (i.e., for GHGs as CO_2-C, CH_4-C and N_2O-N yr^{-1}). Budgets are reported as Tg C or N and are reported as mean fluxes with 95% confidence intervals (CI). In this paper we aim to present the most complete available budget estimates derived

from data-driven ecosystem upscaling (all values from Ramage et al., in prep.), process based models (typically Dynamic Global Vegetation Models, Land Surface Models or ecosystem models) and from atmospheric inversion models. Figure 2 shows a generalized overview of the approach. Consistent with global GHG budgets (Friedlingstein et al., 2022; Saunois et al., 2020; Tian et al., 2020) sinks into the biosphere are reported as negative numbers while sources to the atmosphere are reported as positive numbers. Ecosystem upscaling and process-based model ensembles are considered as bottom-up inventories, while the inverse atmospheric model ensembles are viewed as top-down atmospheric constraints. To estimate the total combined radiative balance of the permafrost region GHG budgets, all budgets are combined to a common unit of CO_2-C equivalents. This is calculated as Global Warming Potential (GWP) for a 100 year time period (GWP-100 from table 7.15 in IPCC, 2023).

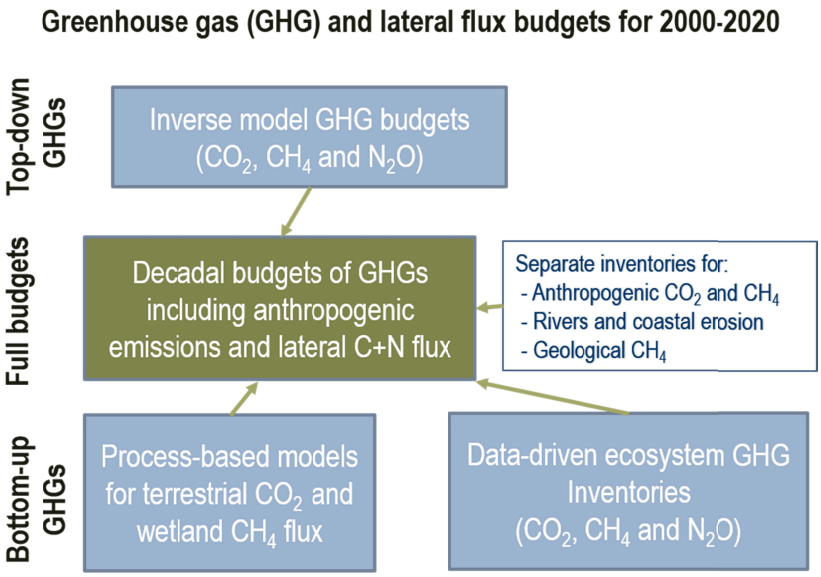

Figure 2: Conceptual figure summarizing the overall approach, including top-down and bottom-up, to compile the RECCAP2 permafrost GHG and lateral flux budgets. Main budget components are presented in blue boxes. The bottom-up process-based models include both ensembles of process-models as well as model-data fusion (MDF) with CARDAMOM. Additional budget components in blue text (white box) include separate inventories of anthropogenic fluxes, lateral fluxes (rivers and coastal erosion) and geological emissions which are used to complete the budgets. Data-driven ecosystem GHG inventories and estimates of lateral fluxes and geological CH4 are taken directly from Ramage et al. (in prep.)

CO_2-C budget from process-based models

Estimates of terrestrial ecosystem fluxes of CO_2 were extracted from an 'ensemble of opportunity' consisting of 73 process-based model simulations that have been generated over the past 10 years as

part of model intercomparison projects. Supplemental table S1 summarizes all the models included, which model intercomparison project they belonged to, the last year of simulation, and whether they represent processes relevant to fires as well as permafrost carbon. These include one variant of each model taken from the available historical simulations in the following projects: the Coupled Model Intercomparison project phase 5 and 6 (CMIP5 and CMIP6) historical coupled climate simulations (Eyring et al., 2016; Taylor et al., 2012) and the Land Surface, Snow and Soil Moisture Model Intercomparison Project (LS3MIP) land-history simulations driven by observed meteorology (Van Den Hurk et al., 2016). These simulations were performed by various modelling groups and are available from either the CMIP5 archive (https://esgf-node.llnl.gov/search/cmip5) or the CMIP6 archive (https://esgf-node.llnl.gov/search/cmip6). We downloaded and extracted carbon stocks and fluxes from both the Permafrost Carbon Network (PCN) and Multi-scale Synthesis and Terrestrial Model Intercomparison Project (MsTMIP) ensembles via the ORNL DAAC (McGuire et al., 2022 and (Huntzinger et al., 2018, respectively). Data from the Inter-Sectoral Impact Model Intercomparison Project phase 2a and 2b (ISIMIP2a and ISIMIP2b) were downloaded from https://www.isimip.org. In the case of ISIMIP2a, only the ensemble members driven by Global Soil Wetness Project version 3 (Dirmeyer et al., 2006) data were included. For ISIMIP2b, only the ensemble members driven by bias-corrected climate data from the IPSL-CM5A-LR Earth System model submitted to the CMIP5 archive were considered. The other available ensemble members were very similar, which, if included, would mean ISIMIP2a/2b would contribute the overall majority of the models to the ensemble of opportunity. Supplemental Table 1 shows which model simulations represent permafrost carbon. Initial results from ISIMIP3a/3b simulations are also shown for four models (i.e., JULES, ORCHIDEE-MICT, JSBACH, and ELM-ECA). Results from these model simulations are previously unpublished and described in more detail in the paragraph below.

The ISIMIP3 modelling output was from:

(i) The Joint UK Land Environment Simulator (JULES) which was driven by GSWP3 meteorology bias corrected by the W5E5 data set (Lange, 2019), denoted GSWP3-W5E5 under the ISIMIP3a protocol. JULES is the land surface component of UKESM (Sellar et al., 2019). The configuration of JULES presented here includes the representation of C and N cycling (Wiltshire et al., 2021) but not vertically resolved soil carbon.

(ii) ORCHIDEE-MICT was also driven by GSWP3-W5E5 following the ISIMIP3a protocol. ORCHIDEE-MICT (Guimberteau et al., 2018) is a version of ORCHIDEE with permafrost C representation in a multilayered vertically discretized model, interactions between soil C, soil temperature and hydrology, and a fire module which burns litter and vegetation. The version used in ISIMIP3a is further improved with representation of grassland management (Chang et al., 2021) and northern peatlands (C. Qiu et al., 2020).

(iii) JSBACH-wet and JSBACH-dry were driven by GFDL-ESM4 historical forcing, following the ISIMIP3b protocol. JSBACH is the land surface component of the Max Planck Institute for Meteorology Earth System Model MPI-ESM version 1.2 (Mauritsen et al., 2019), with methane cycle according to (Kleinen et al., 2020). The "wet" and "dry" configurations cover plausible ranges of soil parameters leading to wetter and dryer soil conditions (De Vrese et al., 2023).

(iv) ELM-ECA was driven by climate data from GFDL-ESM4 submitted to the CMIP6 archive. GFDL-ESM4 was bias-corrected by the W5E5 data that was also used in ISIMIP3a. This simulation follows the ISIMIP3b protocol. ELM-ECA is a land model from the Energy Exascale Earth System Model (E3SM) (Zhu et al., 2019). It simulates C, N, phosphorus, water and energy cycles for major terrestrial ecosystems (e.g., forest, shrub, grassland, wetland). ELM-ECA considers multiple nutrient competitions among plants, microbial immobilizer, nitrifier, denitrifier, and mineral surfaces to resolve the resource partitioning among different competitors. The version used in ISIMIP3b has improved the parameterization on wetland inundation and upland plant carbon-nutrient interactions.

All of the models (supplemental table S1) contain their own individual C cycle processes with a range of complexities. Eighteen of the 73 simulations include a representation of permafrost C and were analysed as a separate sub-ensemble (layered and bulk C, respectively). The multi-annual mean estimate of the carbon stocks and fluxes was defined for the period 1980 to the end of the model simulation (supplemental table S1). The mean residence time of dead organic matter (MRT_{SHR}) is defined as the sum of C stored in SOM and litter content divided by heterotrophic respiration. All of these models estimate the net ecosystem productivity of CO_2 (NEP = NPP - SHR), where NPP is the net primary productivity and SHR is the soil heterotrophic respiration and positive values are a land sink. Some of the process-models used here also consider the additional impact of aboveground C emissions from fire but none estimate belowground C loss from fire. In this case the net biosphere productivity is defined which additionally includes the fire emissions (NPP - SHR - fire). This is of particular note given the majority of fire carbon emissions in the circumpolar domain are from belowground sources: roughly 84-90% in arctic-boreal North America and 57-74% in Eurasia (Potter et al., 2023; Veraverbeke et al., 2021; Walker et al., 2020). Other disturbances, such as pest or storm damage to forests, are not considered here. Fluxes from rivers and lakes are also excluded, as well as those from abrupt permafrost thaw since these processes are not represented by the included models. Carbon use efficiency (CUE), defined as the ratio of net primary productivity (NPP = GPP - plant respiration (R_a)) to GPP, is an emergent property of the models which quantifies vegetation efficiency at storing C fixed via photosynthesis on annual timescales. In addition, full ecosystem budgets for CH_4 and N_2O fluxes from process-based models were either not available or not provided for the model intercomparisons (but see separate section for process-based model budgets of wetland CH_4 flux).

Observation-informed estimates of terrestrial C stocks, fluxes and ecosystem traits (e.g. MRT_{SHR}) within a consistent mass-balanced framework are essential to support evaluation of the model ensembles described above. To generate these estimates we use the CARbon DAta MOdel fraMework (CARDAMOM) (Anthony Bloom et al., 2016), which has been previously used to inform our understanding of Arctic C-cycling (López-Blanco et al., 2019). CARDAMOM is a model-data fusion framework that uses a Bayesian approach within an adaptive-proposal Markov chain Monte Carlo (AP-MCMC) (Haario et al., 2001) to train a process-model of intermediate complexity, DALEC (A. A. Bloom & Williams, 2015; Smallman et al., 2021; Smallman & Williams, 2019). CARDAMOM estimates ensembles of parameter sets for each location independently from each other as a function of location specific data-constraints. These location specific parameter ensembles result in DALEC simulations consistent with the assimilated datasets, their associated uncertainties and ecological and dynamical constraints (for details see Famiglietti et al., 2021). From these parameter ensembles CARDAMOM can generate pixel-level estimates of terrestrial C-cycling and their associated uncertainty, allowing a more rigorous evaluation of more complicated process-oriented models which have a less direct connection to data (Caen et al., 2022). Specifically in this analysis, CARDAMOM analysed terrestrial C-cycling at a monthly time step and 0.5 x 0.5 degree spatial resolution for 19 years (2001-2019). The meteorological drivers were drawn from the GSWP3-W5E5 dataset, while fire was imposed as a function of MODIS burned area (Giglio et al. 2015) and forest loss was constrained using global forest watch (Hansen et al., 2013). Assimilated information was time series estimates of leaf area index (Copernicus Service Information 2021), woody biomass for 2017 and 2018 (Santoro et al., 2021), and net biome exchange of CO_2 (Koren 2020). Moreover, the Northern Circumpolar Soil Carbon Database (NCSCD) provided a pixel specific prior for the initial soil C content (G. Hugelius et al., 2013; G Hugelius et al., 2013). Finally a globally applied prior for the ratio of autotrophic respiration and photosynthesis of 0.46 +/- 0.12 (Collalti & Prentice, 2019). For a more detailed description of CARDAMOM, DALEC and its drivers and observational constraints see the supplemental text and figure S2.

Estimated wetland CH_4 emissions from process based models

Because of limited data availability, no full ecosystem flux budgets of CH_4 from process-based models are available. But there are global-scale estimates of CH_4 budgets for the wetland component of the terrestrial land surface, produced for the Global Methane Budget (Saunois et al., 2020). This study defined wetlands as peatlands (bogs and fens), mineral soil wetlands (swamps and marshes), and seasonal or permanent floodplains. This excludes exposed water surfaces without emergent macrophytes (such as ponds, lakes and rivers) and coastal vegetated ecosystems. In Saunois et al (2020) 13 land surface models which represent CH_4 exchanges were run for the time period 2000-2017, using a common climatic forcing (see table 2 in Saunois et al., 2020). For the permafrost region

budget, only model runs with wetland extent constrained by the Wetland Area Dynamics for Methane Modeling dataset (WAD2M) (Zhang et al., 2021) were used (called "diagnostic model runs" in Saunois et al., 2020). The annual modelled CH_4 wetlands budgets were extracted for the permafrost region and summarised per decade. Although the spatial extent of wetlands in BAWLD is not exactly the same as in WAD2M, the two datasets are similar. They are based on partly identical source data and the definition of wetlands applied in WAD2M is consistent with definitions in BAWLD. We therefore consider the estimates to be sufficiently similar that it supports comparison of CH_4 budgets from ecosystem upscaling with estimates from process-based models (i.e. differences between the methods themselves are much larger than differences in wetland area). Supplementary table S2 summarizes the process-based models used to estimate CH_4 wetland fluxes.

Data driven bottom-up ecosystem GHG budgets and lateral flux budgets

All values reported for data-driven ecosystem flux upscaling of GHG budgets and lateral fluxes presented here are from Ramage et al., (*in prep*). The methods used by Ramage et el., (*in prep*) are briefly described below, but we refer to the original paper for full details.

Ramage et al (*in prep*) calculated C and N budgets (2000-2020) by summing GHG uptake and emissions from terrestrial ecosystems, inland waters, and from disturbances (fire and abrupt thaw), as well as lateral fluxes and geological emissions using several synthesis datasets. The land cover classification used for the analysis was adapted from the BAWLD land cover classification (Olefeldt et al., 2021). The original 19 terrestrial land cover classes in BAWLD were aggregated into five classes: *Boreal forest*, *Non-permafrost wetlands*, *Dry tundra*, *Tundra wetlands* and *Permafrost bogs*. The classes *Dry tundra, Tundra wetlands, and Permafrost bogs* are underlain by surface permafrost and differ largely based on wetness and organic soil depth. Because of spatially discontinuous permafrost coverage, *Boreal forests* include both permafrost and permafrost-free ecosystems. Mean annual fluxes of CO_2, CH_4, and N_2O were obtained for each of the five terrestrial land cover classes by modifying three comprehensive GHG flux dataset compilations for CO_2 fluxes (A.-M. Virkkala et al., 2022), CH_4 fluxes (Kuhn et al., 2021); and for N_2O fluxes (Voigt et al., 2020) (with addition of N_2O fluxes for Boreal forest).

Similarly, inland waters fluxes of CO_2 and CH_4 to the atmosphere were calculated by upscaling mean annual fluxes from lakes and rivers using the estimated surface area of these aquatic classes from the BAWLD classification, adjusted to the permafrost region adjusting for ice-covered duration and fluxes during ice break-up (see Ramage et al., in prep for details). To estimate lake fluxes of N_2O from inland waters, gridded global data of annual flux from (Lauerwald et al., 2019) were used. Estimates of river and stream CO_2 flux were calculated from gridded monthly flux data (Liu et al., 2022) (data from https://doi.org/10.5061/dryad.d7wm37pz9), using adjusted surface areas. Riverine CH_4 emissions were determined using the mean CH_4 diffusive flux reported in the MethDB database

411 (Stanley et al., 2016). To estimate river fluxes of N_2O, gridded global data of annual full landscape
412 flux were used (Maavara et al., 2019).
413 Monthly fire emissions of CO_2 and CH_4 were extracted for the study region from the Global Fire
414 Emission Database version 4s (GFED; van der Werf et al., 2017). The GFED spans from 1997-2016
415 and is driven by estimates of burned areas derived from satellite-based remote sensing data at a spatial
416 resolution of 0.25 degrees (Van Der Werf et al., 2017).
417 Fluxes of CO_2 and CH_4 from landforms caused by abrupt thaw (thermokarst) were extracted from an
418 inventory-based abrupt thaw model (Turetsky et al., 2020), in which emissions are estimated for three
419 generalized types of abrupt thaw terrains: mineral-rich lowlands, uplands/hillslopes, and organic-rich
420 wetlands. The abrupt thaw model was initialized for a historical assessment period (1900-2000) and
421 was then run for the period 2000-2020 to assess CO_2 and CH_4 emissions from active and stabilized
422 abrupt thaw features. To prevent double counting, fluxes from mineral-rich lowlands and organic-rich
423 wetlands were counted as a sub-flux (not added to the total) of terrestrial land cover fluxes.
424 Lateral C and N fluxes from riverine transport and coastal erosion (i.e., DOC and DON losses from
425 the permafrost region to the ocean) are taken from (Terhaar et al., 2021), representative for all land
426 north of 60° N. Emissions from coastal erosion were calculated by multiplying spatially resolved
427 estimates of coastal erosion rates by estimates of C content in coastal soils (Lantuit et al., 2012).
428 Estimates of geological emissions of CH_4 (from subsurface fossil hydrocarbon reservoirs) are taken
429 from an upscaled circumpolar permafrost region estimate for gas seeps along permafrost boundaries
430 and lake beds (Walter Anthony et al., 2012). No separate estimates of geological emission for CO_2 or
431 N_2O are available for the permafrost region.
432

433 ## Combined best-estimate for bottom-up budgets

434 To reconcile the differences between the varying bottom-up approaches integrated bottom-up GHG
435 budgets were created by combining results of the ensembles of process-based models and ecosystem
436 upscaling. The integrated bottom-up estimate is calculated as the mean of the process-based models
437 and ecosystem upscaling for upland and wetland ecosystems, respectively, but adding some
438 components which are lacking in the process-based models. The calculator is based on the subset of
439 the process-based model ensembles which include fire flux. Because inland waters are not included in
440 process-based models the numbers from ecosystem upscaling are added to the total. Because models
441 do not account for abrupt thaw wetlands, estimated fluxes from such processes are added to the
442 budgets from process-model wetland flux (with corrections of model fluxes proportional to the
443 respective areas occupied by inland waters and abrupt thaw wetlands).
444

GHG budgets from atmospheric inversions models

Independent decadal budgets for CO_2, CH_4 and N_2O are derived from ensembles of inverse flux estimates. Budgets for 2000-2010 are reported for all GHGs. Due to differing data availability during the second decade, the GHG budgets are reported for different time periods; 2010-2020 for CO_2, 2010-2017 for CH_4, and 2010-2019 for N_2O. Inverse systems for estimating GHGs vary significantly in the time scale of the analysis, the spatiotemporal resolution of the inferred fluxes, or the inverse modeling framework used (Gaubert et al., 2019; Peylin et al., 2013), all of which result in differences in the inferred flux estimates. To get the best estimates of GHG budget from atmospheric inversion models, a common method is therefore to derive a mean or median flux estimate and the spread among the estimates from the different atmospheric inversion models (Ciais et al., 2022; Philip et al., 2022). The inverse model systems used to derive annual GHG budgets in this study are summarized in supplemental table S3.

The analyses followed the RECCAP2 protocol to estimate CO_2, CH_4 and N_2O fluxes (Ciais et al., 2022). The specific methodology used to calculate the budgets for CO_2, CH_4 and N_2O are described in more detail in (Friedlingstein et al., 2022) for CO_2, (Saunois et al., 2020) for CH_4, and (Tian et al., 2020) for N_2O. These data were retrieved from the GCP/MPI-BGC/RECCAP-2 data portal (https://www.bgc-jena.mpg.de/geodb/) where the total number of inverse modelling estimates available was 6 for CO_2, 22 for CH_4 and 3 for N_2O. For CO_2, these 6 estimates have undergone a spatial adjustment for differences in the used fossil fuel, cement emissions and cement carbonation sink. One additional CO_2 flux estimate was added (Chandra et al., 2022) to make a total of 7, with a strong overlap with the older versions of these systems used in (Z. Liu et al., 2022). Inversion estimates for CO_2 and CH_4 were derived from either in-situ (surface) observations of atmospheric GHG mole fractions or satellite derived total column estimates. Note that satellite estimates of CO_2 and CH_4 are available primarily from 2009 onwards (e.g., from JAXA's GOSAT and NASA's OCO-2 missions). However, among the 22 available estimates for CH_4, there were multiple submissions from the same group using different configurations of the atmospheric data or errors associated with the data. These submissions were first averaged and then the average estimate was used alongside estimates from the other groups. This resulted in 14 final inverse model estimates that were used to calculate the mean CH_4 budget. There is considerable variability between the analysis systems and a comprehensive assessment of accuracy of individual estimates is lacking for CH_4 and N_2O; but (Friedlingstein et al., 2022) provide an assessment of the skill of inversions against independent aircraft observations for CO_2 (for 6 out of the 7 used here). We calculate the budget using the mean annual value from these ensembles of estimates. For estimates of N_2O, the estimates from one model system deviated more than an order of magnitude from the other two systems, and these data were not used further. With these changes, the included number of inverse modelling estimates available were 7, 14 and 2, for CO_2, CH_4 and N_2O, respectively (Supplemental table S2). There was a large variation

in the spatial resolution of inverse model systems. In all cases, the permafrost mask, which was available at ~1°, was regridded to the resolution of the estimates from the individual models, then the flux estimates were sampled using the permafrost mask and finally averaged using area-weighting to generate a single value at monthly time steps for the permafrost study domain. This procedure follows the protocol outlined in previous RECCAP2 studies (Ciais et al., 2021). Supplemental tables S5, S6 and S7 (for CO_2, CH_4 and N_2O, respectively) contain mean monthly GHG fluxes across the full study domain, for each specific inverse model used to calculate decadal means.

Top-down estimated fluxes of CO_2 from fires (not added to the total, reported as sub-flux) are extracted from a separate study combining satellite retrievals and atmospheric inversion of carbon monoxide (CO) converted to CO_2-C emissions using fixed emission factors (Zheng et al., 2023). Gridded estimates of fire CO_2-C fluxes from this study were retrieved (https://doi.org/10.6084/m9.figshare.21770624, resolution of 3.75°×1.9°), clipped to the extent of our study domain and summarized for the relevant time periods. To report separate sub-fluxes of CH_4 from fires, data was extracted from the Global Methane Budget inventory using the *Biomass and biofuel burning* component of the top-down ensemble of global inversion estimates (Saunois et al., 2020), available for 2000-2017. These are inventory-based, but methodologically consistent with the CH_4 inversions.

Anthropogenic emissions

Estimates of anthropogenic CO_2 emissions of fossil fuel combustion (coal, gas and oil estimated separately), cement production and cement carbonization were extracted from the Global Carbon Project's gridded dataset for fossil CO_2 emissions and related O_2 combustion (GCP-GridFED) (M. W. Jones et al., 2021), updated for the 2022 edition of the Global Carbon Budget (GCP-GridFEDv2022.2; Jones et al., 2022). In GCP-GridFED, the emissions of fossil CO_2 relate to the combustion and use of fossil fuels and the production of cement clinkers. These estimates are consistent at the national and annual level with the emissions inventory compiled by the Global Carbon Project (Friedlingstein et al., 2022; Andrew and Peters, 2022). Emissions are gridded at 1 km resolution based on the Emissions Database for Global Atmospheric Research (EDGAR) dataset, version 4.3.2 (Janssens-Maenhout et al., 2019), and distributed across the months of each year using a relationship with heating and cooling degrees (years 1959-2019) and Carbon Monitor to reflect the impact of COVID-19 (year 2020), as described by Jones et al. (2021, 2022).

Estimates of anthropogenic CH_4 emissions were estimated using the *Fossil fuel* plus *Agriculture and waste* components of the top-down ensemble of global inversion estimates from Saunois et al. (2020) (available for 2000-2017). We refer to Saunois et al., (2020) for more details on how these datasets were derived. No separate estimates for anthropogenic N_2O fluxes are included in the study.

Results and discussion

Bottom-up budgets from models and upscaling

Bottom-up ecosystem CO_2 budgets from process-based models

The process-models are divided into two ensembles based on whether they include (*layered C*) or exclude (*bulk C*) an explicit representation of permafrost C (Figure 3). From the 73 available models 55 include permafrost C. The model ensembles are also compared with the observationally-informed CARDAMOM analysis to provide independent quantification of the likelihood of the process-model estimates. Process-model ensemble outputs can be further separated into tundra or boreal, as defined in the BAWLD database (Figures S3 and S4).

The land surface area in the permafrost region is estimated to be a net sink of CO_2 by both model ensembles (including (*layered C*) or excluding (*bulk C*) representation of permafrost C) and the CARDAMOM analysis (Figure 3). When considering net ecosystem productivity (NPP - SHR), the full model ensemble suggests a net sink of -420 (-80 to -1020) Tg CO_2-C y^{-1} with CARDAMOM showing a net uptake of -960 (sink of -1880 to source of 20) Tg CO_2-C y^{-1} (table 1). Out of the 73 process-based model runs, 40 runs did not include fire and as a result are excluded from the net biome productivity (NPP - SHR - F_{fire}) reported (supplemental table S1). The 33 models that include fire, albeit not including combustion of belowground sources, estimate fire emissions of 120 (10 to 460) Tg CO_2-C y^{-1} . This estimate is larger and has a much greater spread than CARDAMOM which has values of 60 (50 to 100) Tg CO_2-C y^{-1}. The inclusion of fire emissions reduces the net land uptake (only the models which include fire emissions) to -340 (-90 to -930) Tg CO_2-C y^{-1}, while CARDAMOM estimates a reduced net land uptake of -870 (sink of -1780 to source of 160) Tg CO_2-C y^{-1} (Figure 3). Although not reflected in the model ensembles, CARDAMOM's ensemble shows the source/sink boundary falls between the 75th and 90th quantile and thus the permafrost region could be a small net source of C.

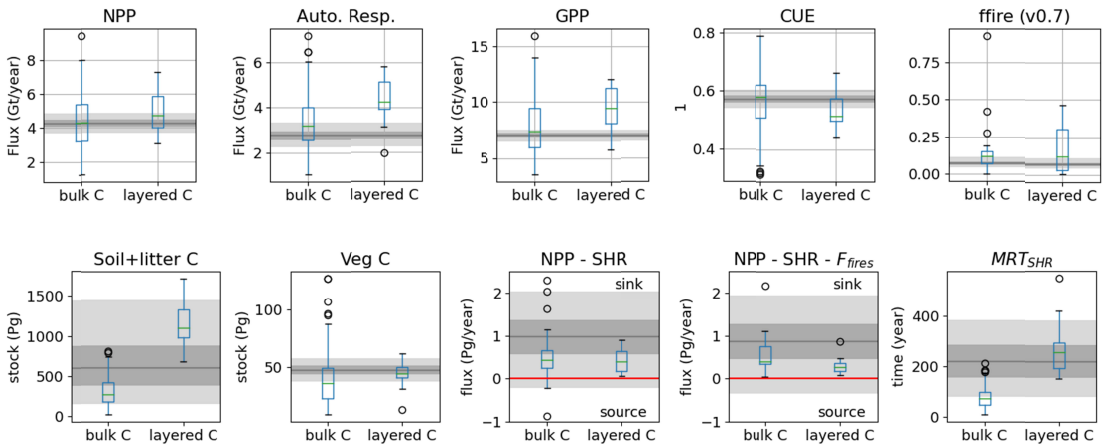

Figure 3. Carbon fluxes, stocks and relevant ecosystem properties from the process-based models listed in supplemental table S1 over the BAWLD region. The top row shows the following simulated multi-annual mean C fluxes (left to right) - heterotrophic respiration (SHR); gross primary productivity (GPP); net primary productivity (NPP); autotrophic respiration (R_a) all in Pg CO_2-C y^{-1}. Also shown on the top row are the carbon use efficiency (CUE, dimensionless) and the fire C flux (F_{fire} in Pg CO_2-C y^{-1}). The bottom row shows C stocks (soil and litter carbon and vegetation carbon, both in Pg C), the net ecosystem productivity (NPP - SHR in Pg CO_2-C y^{-1}); and the net biosphere productivity (NPP - SHR - F_{fire} in Pg CO_2-C y^{-1}) for the models that include fire emissions. The final plot at the bottom right shows the mean residence time of dead organic matter (MRT_{SHR}; years). The model ensemble is divided into two sub ensembles depending on whether they have a representation of permafrost carbon. In each subplot the left hand box plot ("*bulk* C", n=55) represents models without permafrost carbon representation and the right hand box plot ("*layered* C", n=18) represents models which include permafrost carbon. The grey shading represents the likely range estimated by the observationally-informed CARDAMOM analysis. The solid grey line indicates the 50 % quantile, i.e. most likely estimate. The dark grey zone defines the 50 % confidence interval around the 50 % quantile while the light grey zone is the 95 % confidence interval also around the 50 % quantile. In the (NPP - SHR) and (NPP - SHR - F_{fires}) plots the red line is at zero and positive values are a net uptake of carbon.

In terms of the plant based C fluxes (i.e. GPP, R_a, NPP and CUE), there is no significant difference (Mann-Whitney, $p < 0.01$) between the *layered C* models and the *bulk C* models (Figure 3). CARDAMOM's data-informed analysis falls within the spread of the process models. However, the spread of values simulated by the process models is considerably larger than that suggested by CARDAMOM. This is in contrast to the (NPP - SHR) and (NPP - SHR - F_{fires}) fluxes discussed above.

The MRT_{SHR} is significantly longer in models with explicit permafrost C (265 years, *layered C*) than those without (81 year, *bulk C*) (Mann-Whitney $p < 0.01$; Figure 3). Longer MRT_{SHR} in *layered C* models more closely aligns with CARDAMOM's observationally-informed analysis. Furthermore, the overall majority of the *layered C* models fall within CARDAMOM's 95 % CI. The ones that fall outside have a longer MRT_{SHR} than CARDAMOM. In contrast only a small fraction of the *bulk C* models are consistent with the CARDAMOM MRT_{SHR} with the remainder of the models having a shorter MRT_{SHR} than CARDAMOM. The *layered C* models also have a significantly larger soil C

stock which combined with the differences in MRT_{SHR} lead to simulating a similar magnitude of regional heterotrophic respiration as the bulk C models. It is not unexpected that the heterotrophic respiration is similar between the two model ensembles - the additional soil carbon that has been added in the deeper layers is mostly frozen and therefore has very slow heterotrophic respiration. Thus, the *bulk C* models estimate regional heterotrophic respiration which is consistent with both CARDAMOM and *layered C* models but the *layered C* models have the potential for large changes in respiration in the future, whereas the *bulk C* models do not.

The models within this process based model ensemble were run for several different model intercomparison projects so they are not directly comparable in terms of protocol or time period covered. A more constrained ensemble may reduce the uncertainties in the budget estimates. However, the spread of model estimates are still smaller than that from the observationally constrained CARDAMOM assessment.

Bottom-up estimate of natural wetland CH_4 fluxes from process-based models

Full model ensemble budgets are only available for CO_2, but for CH_4 a process-based model ensemble (n=13) of natural wetland CH_4 flux estimates was available from the global CH4 budget (Saunois et al., 2020). The ensemble annual mean is a wetland CH_4 source of 12 (8.6, 16) Tg CH_4-C yr-1 (Table 1). The interannual variability of the ensemble is low (annual means between 11.2 and 14.1), but there is very large spread within the model ensemble, with annual means over the period varying from 4.9 to 28 Tg CH_4-C yr-1 for individual models (table S2).

Bottom-up ecosystem GHG budgets from data driven upscaling

Bottom-up estimates of GHG budgets from data driven upscaling used for the GHG budgets presented here are all based on Ramage et al. (in prep). More in depth results and discussion can be found in that paper. Table 2 summarizes the main findings for the larger budgets posts of the three bottom-up data driven ecosystem GHG budgets from that paper. All numbers are annual means estimated over the full reporting period of 2000-2020.

The total budget of CO_2 is near neutral, but with a large uncertainty range 0.4 (-620, 652) Tg-CO2-C yr-1 (table 2). Sinks of CO_2, mainly in Boreal forest (-270 (-540, -1) Tg-CO_2-C yr-1) and Permafrost-free wetland land cover types (-69 (-125, -14) Tg-CO_2-C yr-1) are offset by sources of CO_2 from fires (109 (84, 135) Tg-CO_2-C yr-1) and inland waters (streams, rivers, lakes and ponds combined; 231 (132, 360) Tg-CO_2-C yr-1). The land cover types Dry tundra ecosystems, Permafrost bogs and Tundra wetlands have CO_2 budgets within ±3 Tg of neutral.

The total bottom-up data driven budget for CH_4 shows a net source of 38 (21, 53) Tg CH_4-C yr-1 (table 2). The strongest CH4 sources are Permafrost-free wetlands and inland waters (21 (14, 27) and 9.4 (4.5, 13) Tg CH_4-C yr-1, respectively). In addition, all other land cover types types, as well as

606 fires and geological emissions, represent weak sources of CH_4 to the atmosphere (from 1.2 to 3.3 Tg
607 CH_4-C yr-1), with the exception of Boreal forests which are a weak sink (-1.1 (-2.2, 0) CH_4-C yr-1).
608 The total bottom-up data driven budget for N_2O shows a net source of 0.62 (0.03, 1.2) Tg N_2O-N yr-1
609 (table 2). All land cover types, and fires represent net sources of N_2O to the atmosphere. The strongest
610 sources are Boreal forest and Dry tundra ecosystems (0.14 (-0.01, 0.3) and 0.23 (0.04, 0.42)Tg N_2O-N
611 yr-1 respectively).
612
613 Table 2. Summary of all main budget posts for the three GHGs from bottom-up ecosystem upscaling as presented by
614 Ramage et al., (in prep).
615 Due to the large formats, tables are submitted in a separate Excel file which is hopefully more
616 convenient

617 Integrated bottom-up budget combining process models and ecosystem upscaling

618 Integrated bottom-up GHG budgets were created by combining results of the ensembles of process-
619 based models and ecosystem upscaling, but adding fluxes from components known to be missing in
620 process-based models (abrupt wetland thaw and inland water fluxes, Table 3). These integrated
621 bottom-up budgets are viewed as a best-estimate of bottom-up methods to be contrasted against the
622 top-down atmospheric inversions constraints.
623 For CO_2, the combined sinks estimated using data-driven upscaling for upland ecosystems and
624 wetlands is somewhat lower than ecosystem sink estimated by the adapted process-based model
625 ensemble estimate (-230 and -293 Tg-CO_2-C yr^{-1}, respectively). When adding inland water fluxes, the
626 integrated bottom up estimate for CO2 is a weak sink with a wide uncertainty range on either side of a
627 neutral budget (-31 (-667, 559) Tg-CO_2-C yr^{-1}). For CH_4 the picture is similar, with the combined sum
628 of data-driven ecosystem types and fires being similar to the combined wetland process-based models
629 plus wetland abrupt thaw fluxes (27 and 31 Tg CH_4-C yr-1, respectively). When adding inland water
630 fluxes the integrated bottom up estimate for CH_4 is a source of 38 (23, 53) Tg-CH_4-C yr^{-1}. For N_2O,
631 only the data-driven upscaling estimate is available, so this is used as a best estimate for the bottom-
632 up budget (a sink of 0.62 (0.03, 1.2) Tg N_2O-N yr-1).
633
634 Table 3. Summary of the different budget components used to generate an integrated bottom-up budget for all three GHGs.
635 Due to the large formats, tables are submitted in a separate Excel file which is hopefully more
636 convenient

Top-down ecosystem GHG budget from atmospheric inversion models

Top-down ecosystem GHG budgets are derived from ensembles of atmospheric inversion model systems. To facilitate comparison to bottom-up estimates, the top-down inversion budgets are ecosystem budgets, excluding anthropogenic emissions (these are reported below).

The ensemble of atmospheric inversion models for CO_2 (n=7) indicates that the ecosystems of the permafrost region is a total net CO_2 sink with a multi-annual mean of -587 (-862, -312) Tg-CO_2-C yr^{-1} (2000-2020, Table 4). Included within this net sink are CO_2 sources from fires, estimated by one inverse model system as 78 (51, 104) Tg-CO_2-C yr^{-1}. The inversion systems shows a stronger mean annual sink in 2010-2020 compared to 2000-2009 (-643 (-917, -369) and -526 (-802, -250) Tg-CO_2-C yr^{-1}, respectively).

The ensemble of inversion models analyzing CH_4 (n=14) shows a multi-annual mean source from natural ecosystems of 15 (11, 18) Tg CH_4-C yr-1 (2000-2017; table 4). This estimated source includes small fluxes from fires (1.4 (1.2,1.6) Tg CH_4-C yr-1).

For N_2O, only two separate inverse model estimates are available and they show a neutral balance or weak source of N_2O, with a multi-annual mean of 0.09 (-0.19, 0.37) Tg N_2O-N yr-1 (table 4). There is no notable difference between the first and second decade for CH_4, but the N_2O source was weaker in 2010-2019 compared to 2000-2009 (Table 4).

Table 4: Summary table of GHG emissions (annual mean and 95% CI) from the RECCAP2 permafrost domain from atmospheric inversion models. The reported inverse model fluxes are the ecosystem fluxes, not including anthropogenic emissions. Sub-fluxes from fires (already included in the total) are also shown for CO_2 and CH_4.

Due to the large formats, tables are submitted in a separate Excel file which is hopefully more convenient

There are no previous studies synthesizing atmospheric inversion model estimates of these three GHGs for permafrost regions, but the results are in line with studies of similar scope. A tundra biome synthesis from the first generation of RECCAP (McGuire et al., 2012) estimated a net CO_2 sink (-120 Tg C yr^{-1}) between 2000-2006 but with very large differences between individual flux estimates in the ensemble (range -440, +210). Since then, more global top-down inverse GHG flux estimates have become available (Friedlingstein et al., 2022), and some recent studies provided GHG budgets for northern regions. (Bruhwiler et al., 2021) analyzed inverse model ensembles across Boreal (50-60 N) and Arctic (60-90 N) domains and describe sinks of CO_2 (-290 and -130 Tg CO_2-C yr^{-1}, respectively for 1980-2017) and sources of CH_4 (16 and 9 Tg CH_4-C yr^{-1}, respectively for 2000-2017). Using a similar time series of estimates from atmospheric inversion models, Liu et al. (2022) found that the permafrost region changed from being CO_2 neutral (1980-2000) to a CO_2 sink in 2000-2017 (ca. -200±100 Tg CO_2-C yr^{-1}). There are no previous atmospheric inverse modelling estimates of N_2O for the permafrost region with which we can compare our results.

Comparison of bottom-up and top-down ecosystem GHG budgets

Synthesis and comparison of the different methods show both convergence and divergence in the different GHG budgets (Figure 4). Below the budgets for individual GHGs as well as total C and N stock change budgets are discussed.

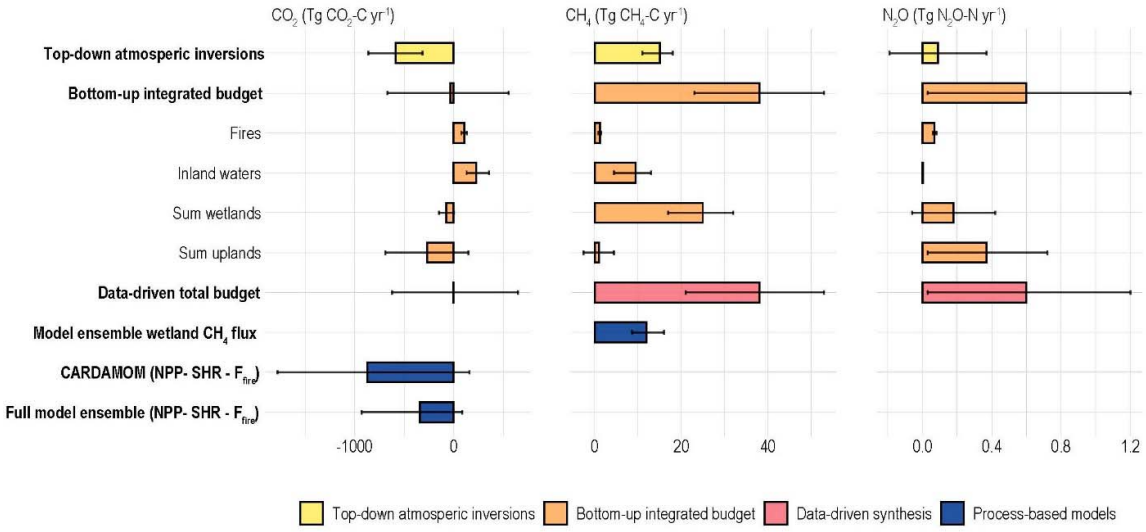

Figure 4. Summary of main budget items for all three GHGs over the time period 2000-2020 calculated using different methods. The error bars represent the 95% confidence interval.

Budgets of CO_2

The CO_2 budget for natural ecosystems (excluding anthropogenic fluxes) using bottom-up approaches is a weak sink of -31 (-667, 559) Tg-CO_2-C yr^{-1} while atmospheric inversion models show a stronger sink of -587 (-862,-312) Tg-CO_2-C yr^{-1}. The 95% CI range of the bottom-up budget is wide and spans across the top-down budget, while the range of the top-down budget is narrower and remains a clear sink. In comparison to top-down and bottom-up budgets, the observationally constrained CARDAMOM system (figure 3, table 1) estimates a stronger sink of CO2 -870 (-1780, 160) Tg-CO_2-C yr^{-1}, but CARDAMOM's ensemble estimates crosses the source/sink boundary between the 75th and 90th quantile and may be consistent with the other bottom-up sources. Especially for the Tundra biome, process-based models (and CARDAMOM) have CO_2 budgets close to neutral, in line with data-driven upscaling for terrestrial land cover types in that region.

Altogether, bottom-up and top-down approaches both show a sink of CO_2 in the region, but of different magnitude, and with some approaches not excluding a shift to a weak source.

Because we present a simplified top-down view in this paper (i.e. no analyses of spatial patterns in individual or ensemble models), it is difficult to pin-point the sources of discrepancies between top-down and bottom-up approaches. However, for the two bottom-up methods of CO_2 budget estimation, the components can be contrasted. Boreal forest and wetland ecosystems are consistent sinks across the bottom-up approaches, but in the integrated bottom-up CO_2 budget, this sink is offset by fluxes from inland waters and fires. Only data-driven upscaling approaches are available to estimate inland water fluxes, which are typically not represented in process-models. If inland waters are excluded from ecosystem upscaling, the net budget for terrestrial land cover types, including fires, is very similar to the (NPP - SHR - Ffire) flux of process models with layered soil C pools (table 3 and figure 3). This suggests that the CO_2 budget for these ecosystems is in agreement between the observational datasets and the generation of models which explicitly represents soil layers and permafrost. It further suggests that process-based models would likely project a weaker CO_2 sink with better representation of inland waters. The three separate methods for calculating fire fluxes spread with estimates of 120, 60, 77 and 110 Tg CO_2-C yr^{-1}, from process-based models, CARDAMOM, one atmospheric inversion, and the GFED inventories respectively. Comparison of different inventories and process-based models in this paper shows that fluxes not represented in the process-based models are potentially large, and should be targeted for inclusion within these complex models. In addition to natural ecosystem fluxes, there may be geological sources of CO_2 which we do not account for, as no separate estimates are available from the permafrost region. The full global geological CO_2 emissions are estimated to 160 Tg CO_2-C yr-1 (Mörner & Etiope, 2002), and it is likely that a small fraction of those fluxes occurs within our study region, but unaccounted for in this budget.

Budgets of CH_4

For the natural balance of CH_4, both the integrated bottom-up budget and the top-down atmospheric inversion models show consistent sources, albeit of different magnitudes at 38 (23, 53) and 15 (11, 18) Tg CH_4-C yr-1, respectively. Even though both the bottom-up and top-down methods show a source of CH_4, their uncertainty ranges do not overlap, suggesting that there may be a systematic bias between the methods.

In the data-driven upscaling, fluxes of CH_4 are characterized by high fluxes per areal unit from the different wetland land cover types, while other classes with more extensive areal coverage such as Boreal forests and Dry tundra are neutral or even weak sinks due to CH_4 oxidation occurring in dry soils. Land cover types with high CH_4 fluxes are often spatially heterogeneous (with large uncertainties in total area of classes) and sometimes fluxes can be especially large along the margins of these land cover patches. These conditions make CH_4 challenging to upscale, and it also means that the spatial landscape heterogeneity, and the spatial resolution of upscaling or modelling becomes very important for determining accurate budgets (Treat et al., 2018a). For inverse models, this scale issue

should not have large effects on how the systems adjust between prior and posterior fluxes. But the resolution and magnitude of the prior flux ensembles may affect the budget.

There are no full CH_4 budgets available from process-based models, but the bottom-up budget includes a model ensemble (n=13) of wetland CH4 flux estimates a source of 12 (8.6, 16) Tg CH_4-C yr-1. This is circa half of the data-driven ecosystem upscaling estimates of combined wetland flux of 25 (17, 32) Tg CH_4-C yr-1. Much of this difference may be explained by the lack of abrupt thaw wetlands in the models, which are included among data-driven land cover types and to the integrated bottom-up budget. In addition, the discrepancy may be partly explained by the poor representation of cold-season methane emissions in process-based models, which tend to be underestimated relative to field-based observations (Treat et al., 2018b). The large differences between estimates suggest that future development of process-based model estimates should target inclusion of inland waters, abrupt thaw, but also upland ecosystems and the potential CH4 oxidation occurring there.

Budgets of N2O

For N_2O, both the bottom-up ecosystem flux upscaling and the top-down atmospheric inversion models show sources but with large differences between estimates (0.62 (0.03, 1.23) and 0.09 (-0.19, 0.37) Tg N_2O-N yr-1, respectively). Both methods have relatively wide uncertainty ranges that overlap each other, and the inverse model estimate cannot with confidence be distinguished from a neutral budget. The bottom-up estimates are seven times higher than the top-down estimates, showing a clear need to further refine the methods and to gather more observational data. The high bottom-up budget is mainly driven by fluxes from large areas of upland Dry tundra and Boreal forest (despite small per unit area fluxes), but uncertainty ranges are wide for all land cover classes and the mean values for classes may be driven up by preferential reporting from measurement sites with high fluxes..

Tian et al., (2020) presented a global quantification of N2O sources and sinks, where top-down and bottom-up estimates were very similar (ca. 17 Tg N_2O-N yr-1) Although they do not present numbers specifically by biome, the estimates for northern regions in Tian et al. (2020) are generally low, and more consistent with our top-down estimates. We provide no model ensemble estimates for N_2O, as few process-based models simulate cycling of N_2O in permafrost ecosystems. One exception is a recent study using the QUINCY model to estimate an average mean annual flux of 4 mg N_2O-N m-2 year-1 across several tundra ecosystem sites (Lacroix et al., 2022). If upscaled to the full tundra domain (5.58 M km2 including classes Wet tundra and Dry tundra), this would yield an annual flux of 0.022 Tg N_2O-N yr-1, an order of magnitude lower than our bottom-up estimates for these same classes. Conversely, another recent model study estimates much higher N_2O fluxes. An ongoing study (in review) uses the TEM model to estimates a pan-Arctic N_2O budget between 1.1 - 1.2 Tg N_2O-N yr-1 (Yuan et al., 2023), which surpasses any previous estimates presented in this study. We note that

767 the cited study is currently in the form of an open discussion paper and we interpret this estimate
768 cautiously. It underscores, however, that the uncertainty of the N_2O budget for the permafrost region
769 is still very large and that modelling work is in its infancy.

770 Anthropogenic CO_2 and CH_4 emissions, lateral export of C and N and total 771 budgets of C

772 Separate estimates of anthropogenic emissions are available from global gridded data for CO_2 and
773 CH_4 (table 5, see table S8 for more details). For both these gases, the emissions are dominated by
774 combustion of fossil fuels occurring within the permafrost region. Anthropogenic emissions of CO2
775 are estimated to be 73 (56, 89) Tg-CO_2-C yr^{-1}, mainly from gas and oil (26 (19, 34) and 32 (27, 36)
776 Tg-CO_2-C yr^{-1}, respectively) (table S8). Anthropogenic emissions of CH4 are estimated to be 5.3 (3.8,
777 6.7) Tg-CH_4-C yr^{-1}, mainly from Fossil fuels but with a small contribution from Agriculture and waste
778 (4.7 (3.4, 6.0) and 0.54 (0.43, 064) Tg-CH_4-C yr^{-1}, respectively) (table S8). These anthropogenic
779 fluxes have not been included to bottom-up and top-down budgets reported above, but are included
780 for total budgets of C as well as calculation of the full combined Global Warming potential of all
781 three GHGs.
782 In addition to the natural and anthropogenic GHG exchange with the atmosphere, C and N is laterally
783 exported from the permafrost region to the Arctic Ocean via riverine transport and coastal erosion
784 (Table 5). The lateral fluxes of organic C were estimated at 94 (79, 110) Tg C y^{-1}, with riverine
785 transport of dissolved organic carbon contributing 78 (70, 87) Tg C y^{-1} and coastal erosion of soil and
786 sediment organic C contributing 15 (9, 24) Tg C y^{-1}. Lateral export of N from the permafrost region
787 is estimated to be 2.6 (1.9, 3.6) Tg N y^{-1} with a smaller component of riverine transport (1.0 (0.9, 1.1)
788 Tg N y^{-1}) compared to coastal erosion (1.6 (1.0, 2.5) Tg N y^{-1}). The ratio of C:N lost via lateral
789 transport is very high (ca. 80) while the C:N ratio in material lost via coastal erosion (ca. 10) is
790 consistent with mature mineral soil organic matter in the permafrost region (Harden et al., 2012).
791 Combining the net CO_2 and CH_4 budgets with lateral fluxes yields annual estimated organic C stock
792 change budgets. The sign and magnitude of combined organic C stock change budgets depend on
793 whether bottom-up or top-down approaches to GHG budgeting are used (101 (-565, 723) and -479 (-
794 772, -183) Tg C y^{-1}, respectively). Using a mean of the bottom-up and top-down budgets for GHGs,
795 we estimate a net sink of C from the atmosphere into the terrestrial permafrost region of -189 (-669,
796 270) Tg C y^{-1}. Because we do not account for all N fluxes, we cannot close the full N budget. Our
797 combined N2O and lateral flux data spreads less between bottom-up and top-down approaches than
798 for C. The mean estimate shows a net loss of nitrogen to the atmosphere and ocean of 2.9 (1.8, 4.4) Tg
799 N y^{-1} (Table 5). As there is a net sink of C in the region, and the overall ecosystem C:N (in soil and
800 vegetation) is unlikely to grow increasingly wider, we expect that if a full N budget was available, a
801 net source of N is more likely. This suggests an unquantified source of N into the system not

quantified in our budgets. If we assume that the total ecosystem C:N ratio (for vegetation and 0-1 m soils) is stable over time at a value around 15-20 (Palmtag et al., 2022), a total N source of 11-14 Tg N y^{-1} would be needed to balance the N budget in relation to the C budget. Likely missing N sources to balance the budget may be atmospheric N deposition or biological N_2 fixation, both important sources of available N for subarctic and arctic ecosystems (Rousk et al., 2018; Yuan et al., 2023). Yuan et al. (2023) report an estimated N deposition between 10 and 15 Tg N yr-1 for the pan-Arctic, in close agreement with the fluxes needed to close the budget. Mean N_2 fixation rates of boreal forest (0.12 g N m-2 y-1) and tundra ecosystems (0.33 g N m-2 y-1) (Yu & Zhuang, 2020) would yield an additional N sinks of 1.2 and 2.1 Tg N yr-1, respectively, if upscaled to the full spatial extent of the Boreal forests and tundra biomes within the region. Although these estimates of additional N sinks into ecosystems are uncertain, they suggest that our estimated net loss of N via N_2O flux and lateral losses from the domain are a small component of the N cycle, and that a balanced full N-budget would be in agreement with an organic C stock change budget based on a GHG C-flux calculated as the mean between bottom-up and top-down approaches.

Table 5. Summary of all main budget posts for the three GHGs, including anthropogenic fluxes as well as lateral fluxes and total sum changes of C and N.

Due to the large formats, tables are submitted in a separate Excel file which is hopefully more convenient

Estimated combined Global Warming Potential of the permafrost region

Using a common unit of CO_2-C equivalents over 100 years (GWP100), and including both ecosystems and anthropogenic emissions, the net balance of the three GHGs from bottom-up approaches shows a net source of 579 (-317, 1432) Tg CO_2-C eq yr^{-1} while top-down atmospheric inversions show a sink of -242 (-576, 83) Tg CO_2-C eq yr^{-1} (Figure 5, Table 6). Using the mean of the two approaches gives an estimated combined GHG source of 147 (-492, 759) Tg CO_2-C eq yr^{-1}). In this mean GWP100 estimate, a CO_2 sink (-237 (-708, 212) Tg CO_2-C eq yr^{-1}) is offset by sources of CH_4 (343 (225, 455) Tg CO_2-C eq yr^{-1}) and N_2O (40 (-9.3, 92) Tg CO_2-C eq yr^{-1})). Our results highlight the importance of monitoring non-CO2 trace gases, since they are responsible for the regions crossing over to a net source of CO_2-C equivalents. Because of their different properties, life times and concentrations in the atmosphere, the total radiative balance of the three GHGs together varies depending on the timescale. Therefore, the estimates of the combined GHG sink or source strengths based on GWP calculations should be interpreted with care. Supplementary table S9 shows a summary of annual GHG budgets converted to CO2-Ceq using 20- and 500-year Global Warming Potential (GWP20 and GWP500). Using CO_2-C equivalents over shorter time-scales (GWP20) yields

net sources from both bottom-up and top-down approaches (1,361 (168, 2512) and 81 (-399, 533), Tg CO_2-C eq yr^{-1} respectively) with a mean source of 721 (-115, 1522) Tg CO_2-C eq yr^{-1}. Over multiple centuries (GWP500), the bottom-up estimate remains a source (124 (-310,)), but both the top-down and mean estimates are of net GHG sinks (-451 (-789, -116) and -132 (-664, 377) Tg CO_2-C eq yr^{-1}, respectively)

The uncertainty ranges of the combined GHG budgets (using GWP100), in both bottom-up and top-down approaches, span across a neutral budget. Because the budget is so close to neutral, recent and future shifts in disturbance regimes may shift the sign of the net GHG budget. The combined effect of fire (from bottom-up scaling) is a source of ca 130 Tg CO_2-Ceq yr^{-1}. Without fires, the mean net GHG balance would be close to neutral, but unusually strong fire years can significantly increase the net GHG source. For instance, in the summer of 2021, global boreal fire emissions were nearly three times larger than the 2000-2020 mean (Zheng et al., 2023). Emissions of CO_2,CH_4, and N_2O from abrupt thaw landforms, both at present and in the future, is a large but highly uncertain source of GHGs. Abrupt thaw (thermokarst) may expand or shift rapidly over time and can be triggered by fires or by unusually warm summers (Turetsky et al., 2020). The estimated fluxes from abrupt thaw lakes and wetlands are conservative in the bottom-up data driven upscaling used for this assessment, but they may be as large as 300 CO_2-Ceq yr-1 for the 2000-2020 period (see Ramage et al. (in prep.))

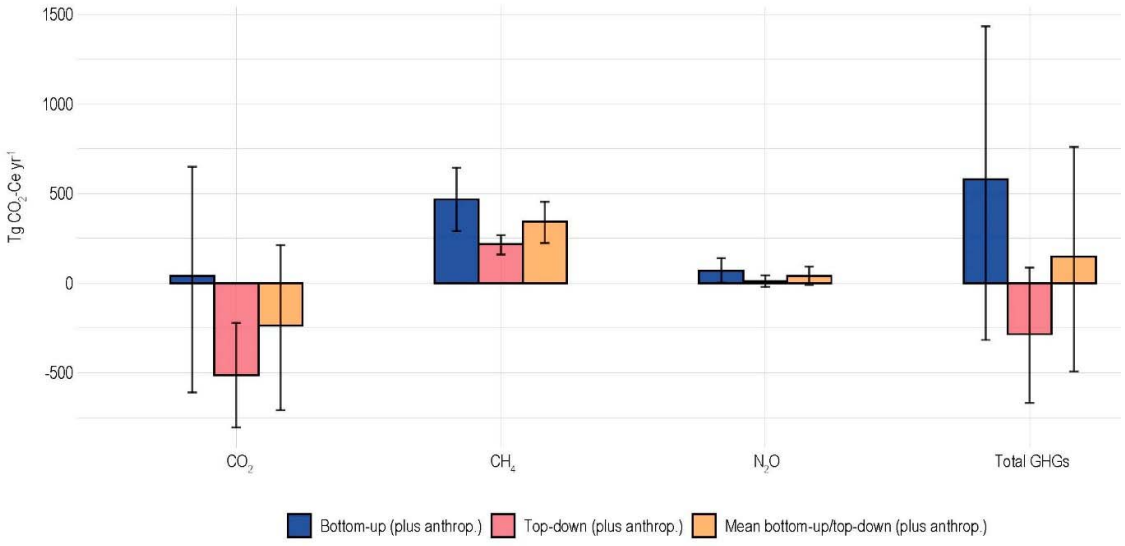

Figure 5. Annual GHGs budgets for bottom-up, top-down approaches, as well as the mean between these two approaches. All numbers converted to CO_2-equivalents (Tg CO_2-Ceq, with 95% CI) using a 100-year Global Warming Potential (GWP-100). Table 6 complements this figure by showing more detailed sub-fluxes for the different categories.

Table 6. Summary of annual GHGs budgets for all main budget posts, converted to CO_2-equivalents (Tg CO_2-Ceq, with 95% CI) using a 100-year Global Warming Potential (GWP-100) from bottom-up approaches, top-down atmospheric

inversion models and from anthropogenic fluxes. A GWP-100 of 29.8 for CH_4 and 273 or N_2O relative to CO2 was used (IPCC, 2023; Table 7.15).

Due to the large formats, tables are submitted in a separate Excel file which is hopefully more convenient

Main sources of uncertainty within and between GHG budgets

The spread between methods in this study is smaller than in some earlier studies (McGuire et al., 2012; Saunois et al., 2020), the differences between bottom-up and top-down estimates are substantial. Combined for all three GHGs over natural ecosystems, the bottom-up ecosystem scaling predicts a source of 449 (-415, 1272) Tg CO_2-Ceq yr-1 while the top-down inversions estimate a sink of -414 (-765, -74) Tg CO_2-Ceq yr-1 (table 6, excluding anthropogenic fluxes). Both the systematic discrepancies between bottom-up and top-down methods, and the wide uncertainty ranges of data and model estimates point to a need for further refinement of methods, process representation and additional observational data.

The flux estimates from the global GHG inversions for the permafrost region show a relatively large spread between the different systems (tables S5-S7). This large range may partly be explained by a relatively limited set of atmospheric concentration observations being available for the region (from the surface networks or satellite observing systems). Furthermore, the resolution at which fluxes are estimated is relatively coarse in comparison to the large landscape heterogeneity of the studied region - this might increase variability between different inversion systems and contribute to the systematic differences in relation to bottom-up approaches.

For all three GHGs, the ecosystem flux upscaling estimates suggest stronger sources than the atmospheric inverse models. Because the budgets presented here integrate the full permafrost domain, it is challenging to assess where and why differences occur between bottom-up and top-down estimates. These consistent differences between bottom-up and top-down methods may indicate a systematic bias in either or both of the methods, possibly related to the representativeness of the observations used, as atmospheric mole fraction measurements have a larger footprint compared to EC observations. Strong sources and sinks of all GHGs are associated with certain land cover classes, land forms or processes (e.g. wetlands, inland waters, thermokarst lakes, and fires). It would be of interest for further studies to analyze the spatial patterns of inversion budgets relative to the distribution of specific land cover types or processes in the landscape.

A potential source of mismatch between bottom-up and top-down estimates is the source of information used to estimate prior fluxes for the GHG inversion systems. It is possible that if prior flux ensembles consistently included all of the land cover types and processes included in bottom-up estimates, they would be more similar. For instance, the global inversions do not include emissions from inland water as prior knowledge for the inversion system (supplemental table S3 and references

898 therein). For CO_2 the prior fluxes are based on land surface models and fire inventories as well as
899 anthropogenic emissions, with systems optimized to estimate fluxes from the natural ecosystems
900 (Friedlingstein et al., 2022). For CH_4, the prior fluxes included only emissions estimated from
901 process-based models for wetlands and anthropogenic sources (Saunois et al., 2020). Inland waters
902 are important sources of all GHGs, with a combined emission of 330 (180, 500) Tg CO_2-Ceq yr^{-1}
903 (Table 6). Adding inland water emissions to the prior flux ensemble may help reconcile bottom-up
904 and top-down estimates. We note that the budgets estimated by the inversion ensembles are relatively
905 similar to the budgets estimated process-based models which have been used as priors. The NEE as
906 well as wetland CH_4 fluxes derived from process-model ensembles are similar to the atmospheric
907 inverse model CO_2 and CH_4 budgets, respectively (-420 and -587 Tg CO_2-C y^{-1} as well as 12 and 15
908 Tg CH_4-C yr-1, respectively). It is possible that in regions with limited atmospheric observations to
909 correct concentration, the posterior inverse model fluxes do not deviate much from the priors. This
910 problem may be particularly important during the long cold season. Shoulder-seasons and winter
911 fluxes of both CO_2 and CH_4 are significant parts of the annual budgets in field measurements across
912 multiple sites but process-based models (used as inversion priors) capture these emissions poorly
913 (Natali et al., 2019; Treat, et al., 2018b). This bias may be further exacerbated by systematic lack of
914 observational constraints during winter. The observational networks for GHG fluxes in the permafrost
915 region during winter are very sparse, especially in Canada and Russia (Pallandt et al., 2022). Further,
916 the inverse model systems that use satellite instruments need enough insolation to measure the CO_2 or
917 CH_4 atmospheric columns. In practice, this restriction means that the high latitudes are rarely sampled
918 by satellites around the winter hemisphere.
919 But even with updated prior fluxes, it is probable that estimates from bottom-up approaches would
920 still be higher than the atmospheric constraint and the balance of global GHG budgets. This suggests a
921 need for further revising the bottom-up upscaling methods in parallel with development of top-down
922 methods and datasets. The spatial products used to delineate the surface area of land cover types for
923 this study remain coarse (Olefeldt et al., 2021), both in terms of spatial resolution and the diversity of
924 land form classes (Ramage et al., in prep). The next generation of remote sensing products are likely
925 to improve estimates of areas of different important land cover classes in the near future. In addition
926 to uncertain areal coverage of key land cover classes, the bottom-up budgets for all GHGs are strongly
927 affected by average fluxes from individual landcover classes. Because of the heterogeneous nature of
928 GHG fluxes in both space and time, it is challenging to generate datasets with unbiased and accurate
929 annual GHG budgets (Rößger et al., 2019; Treat, et al., 2018a). There is a risk of biases toward
930 measurements of high fluxes associated with spatial and temporal variability both within and across
931 landcover types. There is also a risk for higher reporting prevalence from sites with high emissions, or
932 that land cover types that may be weak sinks of GHGs (but may cover large areas) are under-reported.
933 For example, the importance of spatially widespread but weak soil CH_4 sinks in determining the full
934 landscape CH_4 budget has been shown for Arctic tundra in Greenland and Siberia (Juncher Jørgensen

et al., 2015; Juutinen et al., 2022). Larger regional gaps in observational flux networks may also be important (Pallandt et al., 2022; Virkkala et al., 2018), because different regions can have highly diverse environmental conditions and rates of warming and permafrost thaw which can impact GHG fluxes in various ways. The formation and past history of permafrost deposits in different regions also influence the potential permafrost GHG feedback strengths (Jones et al., 2023), which may bias estimates if field data is unevenly spaced. Better representation is also needed from sites affected by different disturbance regimes. This includes both fluxes from disturbance events as well as post-disturbance trajectories, such as CO2 sinks after fire (Walker et al., 2019) or biological pest outbreaks (Lund et al., 2017). If the assemblage of sites used for calculating average GHG fluxes is not broadly representative of areas in long-term recovery trajectories, it may well underestimate C sinks in post-disturbance ecosystems. Another large source of uncertainty is how abrupt permafrost thaw affects GHG budgets. In our budgets, it is partly included in the data-driven upscaling (via specific land cover or lake types types in BAWLD), but entirely missing in the process models. The spatial extent and annual fluxes of abrupt thaw landforms remain poorly constrained (Turetsky et al., 2020). In addition, abrupt thaw landforms and other disturbed soils may emit N_2O (Voigt et al., 2020), but this is not included in any of our budgeting approaches. Further improvements to data-driven bottom-up budgets could be made by i) an increased number of observations, including more spatially distributed data and non-growing season measurements, ii) consistent reporting of net-zero or negative fluxes to prevent biased site selection and reporting in published literature and iii) upscaling using techniques that can simultaneously consider several environmental conditions and their variability across the entire permafrost region (Hugelius et al., 2020; Natali et al., 2019; Virkkala et al., 2021)

Conclusions

We present the first synthesis of GHG budgets for CO_2, CH_4 and N_2O as well lateral fluxes of C and N across the northern terrestrial permafrost region using bottom-up (ecosystem flux upscaling and process-based models) and top-down (atmospheric inversion models) approaches for the period 2000-2020. In comparison, bottom-up approaches consistently yield estimates of stronger GHG sources compared to top-down. Both approaches show a net sink of CO_2 in natural ecosystems, but they diverge by several hundred Tg CO_2-C yr-1 (-31 (-667, 559) and -587 (-862, -312), respectively). The Boreal biome, especially Boreal forest land cover, is a stronger net sink while the tundra biome is neutral, or even a source when accounting for fluxes from inland waters. Bottom-up and top-down approaches both show sources of CH_4, but the 95% CI ranges do not overlap (38 (23, 53) and 15 (11, 18) Tg CH4-C yr-1, respectively). The strongest sources of CH_4 are permafrost-free wetlands, and inland waters. Estimates of N_2O are highly uncertain, but both methods estimate sources to the atmosphere (0.6 (0.03, 1.2) and 0.09 (-0.19, 0.37) Tg N_2O-N yr-1). Anthropogenic emissions from the region are 73 (56, 89) Tg CO_2-C yr-1 and 5.4 (3.8, 7.1) Tg CH_4-C yr-1, in both cases dominated by

combustion of fossil fuels (estimates not available for N2O). Assuming equal weight to bottom-up and top-down budgets, the combined global warming potential at a 100 year timescale (GWP100) is a net GHG source of 147 (-492, 759) Tg CO_2-Ceq yr-1, The CO_2 sink is more than offset by the CH_4 source, with a small source contribution from N_2O (-285, 343 and 40 Tg CO_2-Ceq yr-1, respectively). When calculating global warming potential over decadal time-scales (GWP20) both bottom-up and top-down approaches show net sources of GHGs. The estimated total annual budgets of C and N, when anthropogenic and lateral fluxes are included (but not accounting for N deposition or N2 fluxes), are -189 (-669, 270) Tg C yr–1 and 2.9 (1.8, 4.4) Tg N yr-1.

Inverse model datasets have not been extensively used for studies of the permafrost region, but are highly useful for broad-scale budgets and should be utilized to a greater degree in future studies. The consistently lower land to atmosphere fluxes from top-down inversions compared to bottom up points to potential systematic biases in both methods. Future efforts should focus on improved observational networks to support atmospheric inversions in the region and comparison of spatial patterns within atmospheric inversion models, including analysis of how prior fluxes affect the posterior budgets. Data-driven bottom-up estimates are still data-limited and further refinement of the spatial resolution and GHG balances for individual classes could improve estimates. Process-based model estimates are highly useful and complementary to other budgeting approaches. With future addition or improvement of key processes, such as fire, abrupt thaw and inland water dynamics, it is likely that budgets from process-based models would be similar to data-driven upscaling. If it can be shown that process-based models mimic data-constrained estimates for present day budgets, it increases confidence in using models for projections of future GHG dynamics.

In summary, we cannot currently reconcile bottom-up and top-down GHG budgets for the permafrost region. The bottom-up budget may be biased in ways that increase estimated fluxes to the atmosphere from high-emitting land cover types while top-down atmospheric inversion budgets may be biased in ways that decrease fluxes to the atmosphere by not including ecosystem types that are known net GHG sources in prior flux estimates. Considering these constraints, a mean between the integrated bottom-up and top-down budget approaches can be seen as the most robust best estimate under the current state of knowledge. We conclude that while uncertainties remain, the budgets are sufficiently well constrained to shows the northern permafrost region as a net sink of organic C, but a net source of combined global warming potential over decadal to century time-scales. The boreal biome is likely a GHG sink, or neutral, but the tundra biome is a GHG source. Ongoing and projected future permafrost thaw as well as intensification of disturbance regimes, including droughts, storms, pests and fires are likely to strengthen GHG sources across the whole region.

Acknowledgements

This work is a collaborative effort from the Global Carbon Project Second REgional Carbon Cycle and Processes study (RECCAP2) and contributes to the Arctic Methane and Permafrost Challenge (AMPAC). JR and GH acknowledge support from the European Union's Horizon 2020 Research and Innovation Programme to the Nunataryuk project (no. 773421) and support from the AMPAC-Net project funded by the European Space Agency (ESA). GH acknowledges the Swedish Research Council VR (grant # 2022-04839). JR received additional funding from the Swedish Academy of Science (Formas) under the grant number FR-2021/0004. EJB has received funding from the European Union's Horizon 2020 research and innovation programme under Grant Agreement No 101003536 (ESM2025 - Earth System models for the Future) and from the Joint UK BEIS/Defra Met Office Hadley Centre Climate Programme (GA01101). Work of AC and JL was conducted at the Jet Propulsion Laboratory, California Institute of Technology, under a contract with the National Aeronautics and Space Administration (80NM0018D0004), and additionally AC was supported by NASA Grant/Cooperative Agreement Number: NNX17AD69A. Work of MEM was supported by the Academy of Finland in the frame of the Atmosphere and Climate Competence Center (ACCC) (no. 337550). CV was supported by the Academy of Finland project MUFFIN (grant no. 332196). CB wishes to thank the Academy of Finland (project N-PERM - decision no 341348, project NOCA - decision no. 314630 and the Yedoma-N project decision no. 287469)) for financial support, as well as the PERNO project supported by FWF, Austia (grant # M03335). AMV, BMR, SMN, JDW, and SP were funded by the Gordon and Betty Moore foundation (grant #8414) and through funding catalyzed by the Audacious Project (Permafrost Pathways). MAK was supported by the NSF PRFB Program (Abstract # 2109429). TK acknowledges support through the project Palmod, funded by the German Federal Ministry of Education and Research (BMBF), Grant No. 01LP1921A. JGC was funded by the Australian National Environmental Science Program (NESP2) - Climate Systems Hub. MIROC4-ACTM inversion activity is supported by the Arctic Challenge for Sustainability phase II (ArCS-II; JPMXD1420318865) Projects of the Ministry of Education, Culture, Sports, Science and Technology (MEXT), and Environment Research and Technology Development Fund (JPMEERF21S20800) of the Environmental Restoration and Conservation Agency of Japan. TLS, PIP and LF are supported by the UK National Centre for Earth Observation funded by the Natural Environment Research Council (NE/R016518/1 and NE/N018079/1). The CARDAMOM analyses made use of resources provided by the Edinburgh Compute and Data Facility (EDCF) (http://www.ecdf.ed.ac.uk). The CARDAMOM-permafrost dataset can be freely downloaded from https://doi.org/10.7488/ds/7505. ELB considers this study a contribution to GreenFeedBack (Greenhouse gas fluxes and earth system feedbacks) funded by the European Union's HORIZON research and innovation program under grant agreement No 101056921. EAGS was funded by NSF PLR Arctic System Science Research Networking

Activities (RNA) Permafrost Carbon Network: Synthesizing Flux Observations for Benchmarking Model Projections of Permafrost Carbon Exchange (2019-2023) Grant#1931333. RL acknowledges support by the CLAND convergence institute (16-CONV-0003) funded by the French National Research Agency (ANR). Inversion studies of YN were funded by the Environment Research and Technology Development Fund (JPMEERF21S20800) of the Environmental Restoration and Conservation Agency provided by Ministry of the Environment of Japan, and supported by the NIES and MRI supercomputer systems (NEC SX-Aurora TSUBASA and FUJITSU PRIMERGY CX2550M5). WP and IL acknowledge support for using HPC cluster Aether at the University of Bremen, financed by DFG within the scope of the Excellence Initiative. JC acknowledge support from the National Key Research and

Development Program of China (2022YFF0801904).

References

Aas, K. S., Martin, L., Nitzbon, J., Langer, M., Boike, J., Lee, H., et al. (2019). Thaw processes in ice-rich permafrost landscapes represented with laterally coupled tiles in a land surface model. *The Cryosphere*, *13*(2), 591–609. https://doi.org/10.5194/tc-13-591-2019

Abbott, B. W., Jones, J. B., Schuur, E. A. G., Chapin III, F. S., Bowden, W. B., Bret-Harte, M. S., et al. (2016). Biomass offsets little or none of permafrost carbon release from soils, streams, and wildfire: an expert assessment. *Environmental Research Letters*, *11*(3), 034014. https://doi.org/10.1088/1748-9326/11/3/034014

Andrew, Robbie M., & Peters, Glen P. (2022). The Global Carbon Project's fossil CO2 emissions dataset (2022v27) [Data set]. Zenodo. https://doi.org/10.5281/zenodo.7215364

Biskaborn, B. K., Smith, S. L., Noetzli, J., Matthes, H., Vieira, G., Streletskiy, D. A., et al. (2019). Permafrost is warming at a global scale. *Nature Communications*, *10*(1), 264. https://doi.org/10.1038/s41467-018-08240-4

Bloom, A. A., & Williams, M. (2015). Constraining ecosystem carbon dynamics in a data-limited world: integrating ecological "common sense" in a model–data fusion framework. *Biogeosciences*, *12*(5), 1299–1315. https://doi.org/10.5194/bg-12-1299-2015

Bloom, A. Anthony, Exbrayat, J.-F., Van Der Velde, I. R., Feng, L., & Williams, M. (2016). The decadal state of the terrestrial carbon cycle: Global retrievals of terrestrial carbon allocation, pools, and residence times. *Proceedings of the National Academy of Sciences*, *113*(5), 1285–1290. https://doi.org/10.1073/pnas.1515160113

Brown, D. R. N., Jorgenson, M. T., Douglas, T. A., Romanovsky, V. E., Kielland, K., Hiemstra, C., et al. (2015). Interactive effects of wildfire and climate on permafrost degradation in Alaskan lowland forests. *Journal of Geophysical Research: Biogeosciences*, *120*(8), 1619–1637. https://doi.org/10.1002/2015JG003033

Bruhwiler, L., Parmentier, F.-J. W., Crill, P., Leonard, M., & Palmer, P. I. (2021). The Arctic Carbon Cycle and Its Response to Changing Climate. *Current Climate Change Reports*, *7*(1), 14–34. https://doi.org/10.1007/s40641-020-00169-5

Caen, A., Smallman, T. L., De Castro, A. A., Robertson, E., Von Randow, C., Cardoso, M., & Williams, M. (2022). Evaluating two land surface models for Brazil using a full carbon cycle benchmark with uncertainties. *Climate Resilience and Sustainability*, *1*(1), e10. https://doi.org/10.1002/cli2.10

Canadell, J.G., P.M.S. Monteiro, M.H. Costa, L. Cotrim da Cunha, P.M. Cox, A.V. Eliseev, S. Henson, M. Ishii, S. Jaccard, C. Koven, A. Lohila, P.K. Patra, S. Piao, J. Rogelj, S. Syampungani, S. Zaehle, and K. Zickfeld (2021) Global Carbon and other Biogeochemical Cycles and Feedbacks Supplementary Material. In Climate Change 2021: The Physical Science Basis. Contribution of Working Group I to the Sixth Assessment Report of the Intergovernmental Panel on Climate Change [Masson-Delmotte, V., P. Zhai, A. Pirani, S.L. Connors, C. Péan, S. Berger, N. Caud, Y. Chen, L. Goldfarb, M.I. Gomis, M. Huang, K. Leitzell, E. Lonnoy, J.B.R. Matthews, T.K. Maycock, T. Waterfield, O. Yelekçi, R. Yu, and B. Zhou (eds.)]. Available from https://www.ipcc.ch/

Chandra, N., Patra, P. K., Niwa, Y., Ito, A., Iida, Y., Goto, D., et al. (2022). Estimated regional CO_2 flux and uncertainty based on an ensemble of atmospheric CO_2 inversions. *Atmospheric Chemistry and Physics*, *22*(14), 9215–9243. https://doi.org/10.5194/acp-22-9215-2022

Chang, J., Ciais, P., Gasser, T., Smith, P., Herrero, M., Havlík, P., et al. (2021). Climate warming from managed grasslands cancels the cooling effect of carbon sinks in sparsely grazed and natural grasslands. *Nature Communications*, *12*(1), 118. https://doi.org/10.1038/s41467-020-20406-7

Ciais, P., Bastos, A., Chevallier, F., Lauerwald, R., Poulter, B., Canadell, J. G., et al. (2022). Definitions and methods to estimate regional land carbon fluxes for the second phase of the REgional Carbon Cycle Assessment and Processes Project (RECCAP-2). *Geoscientific Model Development*, *15*(3), 1289–1316. https://doi.org/10.5194/gmd-15-1289-2022

Collalti, A., & Prentice, I. C. (2019). Is NPP proportional to GPP? Waring's hypothesis 20 years on. *Tree Physiology*, *39*(8), 1473–1483. https://doi.org/10.1093/treephys/tpz034

De Vrese, P., Georgievski, G., Gonzalez Rouco, J. F., Notz, D., Stacke, T., Steinert, N. J., et al. (2023). Representation of soil hydrology in permafrost regions may explain large part of inter-model spread in simulated Arctic and subarctic climate. *The Cryosphere*, *17*(5), 2095–2118. https://doi.org/10.5194/tc-17-2095-2023

Dinerstein, E., Olson, D., Joshi, A., Vynne, C., Burgess, N. D., Wikramanayake, E., et al. (2017). An Ecoregion-Based Approach to Protecting Half the Terrestrial Realm. *BioScience*, *67*(6), 534–545. https://doi.org/10.1093/biosci/bix014

Dirmeyer, P. A., Gao, X., Zhao, M., Guo, Z., Oki, T., & Hanasaki, N. (2006). GSWP-2: Multimodel Analysis and Implications for Our Perception of the Land Surface. *Bulletin of the American Meteorological Society*, *87*(10), 1381–1398. https://doi.org/10.1175/BAMS-87-10-1381

Eyring, V., Bony, S., Meehl, G. A., Senior, C. A., Stevens, B., Stouffer, R. J., & Taylor, K. E. (2016). Overview of the Coupled Model Intercomparison Project Phase 6 (CMIP6) experimental design and organization. *Geoscientific Model Development*, *9*(5), 1937–1958. https://doi.org/10.5194/gmd-9-1937-2016

Famiglietti, C. A., Smallman, T. L., Levine, P. A., Flack-Prain, S., Quetin, G. R., Meyer, V., et al. (2021). Optimal model complexity for terrestrial carbon cycle prediction. *Biogeosciences*, *18*(8), 2727–2754. https://doi.org/10.5194/bg-18-2727-2021

Foster, A. C., Wang, J. A., Frost, G. V., Davidson, S. J., Hoy, E., Turner, K. W., et al. (2022). Disturbances in North American boreal forest and Arctic tundra: impacts, interactions, and responses. *Environmental Research Letters*, *17*(11), 113001. https://doi.org/10.1088/1748-9326/ac98d7

Friedlingstein, P., Jones, M. W., O'Sullivan, M., Andrew, R. M., Bakker, D. C. E., Hauck, J., et al. (2022). Global Carbon Budget 2021. *Earth System Science Data*, *14*(4), 1917–2005. https://doi.org/10.5194/essd-14-1917-2022

Gaubert, B., Stephens, B. B., Basu, S., Chevallier, F., Deng, F., Kort, E. A., et al. (2019). Global atmospheric CO₂ inverse models converging on neutral tropical land exchange, but disagreeing on fossil fuel and atmospheric growth rate. *Biogeosciences*, *16*(1), 117–134. https://doi.org/10.5194/bg-16-117-2019

Giglio, L., Justice, C., Boschetti, L., Roy, D. (2015). MCD64A1 MODIS/Terra+Aqua Burned Area Monthly L3 Global 500m SIN Grid V006 [Data set]. NASA EOSDIS Land Processes Distributed Active Archive Center. Accessed 2023-09-01 from https://doi.org/10.5067/MODIS/MCD64A1.006

Guimberteau, M., Zhu, D., Maignan, F., Huang, Y., Yue, C., Dantec-Nédélec, S., et al. (2018). ORCHIDEE-MICT (v8.4.1), a land surface model for the high latitudes: model description and validation. *Geoscientific Model Development*, *11*(1), 121–163. https://doi.org/10.5194/gmd-11-121-2018

Haario, H., Saksman, E., & Tamminen, J. (2001). An Adaptive Metropolis Algorithm. *Bernoulli*, *7*(2), 223. https://doi.org/10.2307/3318737

Hansen, M. C., Potapov, P. V., Moore, R., Hancher, M., Turubanova, S. A., Tyukavina, A., et al. (2013). High-Resolution Global Maps of 21st-Century Forest Cover Change. *Science*, *342*(6160), 850–853. https://doi.org/10.1126/science.1244693

Holloway, J. E., Lewkowicz, A. G., Douglas, T. A., Li, X., Turetsky, M. R., Baltzer, J. L., & Jin, H. (2020). Impact of wildfire on permafrost landscapes: A review of recent advances and future

prospects. *Permafrost and Periglacial Processes*, *31*(3), 371–382. https://doi.org/10.1002/ppp.2048

Hugelius, G., Bockheim, J. G., Camill, P., Elberling, B., Grosse, G., Harden, J. W., et al. (2013). A new data set for estimating organic carbon storage to 3 m depth in soils of the northern circumpolar permafrost region. *Earth System Science Data*, *5*(2), 393–402. https://doi.org/10.5194/essd-5-393-2013

Hugelius, G, Tarnocai, C., Broll, G., Canadell, J. G., Kuhry, P., & Swanson, D. K. (2013). The Northern Circumpolar Soil Carbon Database: spatially distributed datasets of soil coverage and soil carbon storage in the northern permafrost regions, 11.

Hugelius, Gustaf, Strauss, J., Zubrzycki, S., Harden, J. W., Schuur, E. A. G., Ping, C.-L., et al. (2014). Estimated stocks of circumpolar permafrost carbon with quantified uncertainty ranges and identified data gaps. *Biogeosciences*, *11*(23), 6573–6593. https://doi.org/10.5194/bg-11-6573-2014

Hugelius, Gustaf, Loisel, J., Chadburn, S., Jackson, R. B., Jones, M., MacDonald, G., et al. (2020). Large stocks of peatland carbon and nitrogen are vulnerable to permafrost thaw. *Proceedings of the National Academy of Sciences*, *117*(34), 20438–20446. https://doi.org/10.1073/pnas.1916387117

Huntzinger, D. N., SCHWALM, C. R., WEI, Y., COOK, R. B., MICHALAK, A. M., SCHAEFER, K., et al. (2018). NACP MsTMIP: Global 0.5-degree Model Outputs in Standard Format, Version 1.0. ORNL Distributed Active Archive Center. https://doi.org/10.3334/ORNLDAAC/1225

Janssens-Maenhout, G., Crippa, M., Guizzardi, D., Muntean, M., Schaaf, E., Dentener, F., et al. (2019). EDGAR v4.3.2 Global Atlas of the three major greenhouse gas emissions for the period 1970–2012. *Earth System Science Data*, *11*(3), 959–1002. https://doi.org/10.5194/essd-11-959-2019

Jones, M. C., Grosse, G., Treat, C., Turetsky, M., Anthony, K. W., & Brosius, L. (2023). Past permafrost dynamics can inform future permafrost carbon-climate feedbacks. *Communications Earth & Environment*, *4*(1), 272. https://doi.org/10.1038/s43247-023-00886-3

Jones, M. W., Andrew, R. M., Peters, G. P., Janssens-Maenhout, G., De-Gol, A. J., Ciais, P., et al. (2021). Gridded fossil CO2 emissions and related O2 combustion consistent with national inventories 1959–2018. *Scientific Data*, *8*(1), 2. https://doi.org/10.1038/s41597-020-00779-6

Jones, Matthew William, Andrew, Robbie M., Peters, Glen P., Janssens-Maenhout, Greet, De-Gol, Anthony J., Dou, Xinyu, Liu, Zhu, Pickers, Penelope, Ciais, Philippe, Patra, Prabir K., Chevallier, Frederic, & Le Quéré, Corinne. (2022). Gridded fossil CO2 emissions and related O2 combustion consistent with national inventories (GCP-GridFEDv2022.2) [Data set]. Zenodo. https://doi.org/10.5281/zenodo.7016360

Juncher Jørgensen, C., Lund Johansen, K. M., Westergaard-Nielsen, A., & Elberling, B. (2015). Net regional methane sink in High Arctic soils of northeast Greenland. *Nature Geoscience*, *8*(1), 20–23. https://doi.org/10.1038/ngeo2305

Juutinen, S., Aurela, M., Tuovinen, J.-P., Ivakhov, V., Linkosalmi, M., Räsänen, A., et al. (2022). Variation in CO_2 and CH_4 fluxes among land cover types in heterogeneous Arctic tundra in northeastern Siberia. *Biogeosciences*, *19*(13), 3151–3167. https://doi.org/10.5194/bg-19-3151-2022

Kleinen, T., Mikolajewicz, U., & Brovkin, V. (2020). Terrestrial methane emissions from the Last Glacial Maximum to the preindustrial period. *Climate of the Past*, *16*(2), 575–595. https://doi.org/10.5194/cp-16-575-2020

Koren, G. (2020). Constraining the exchange of carbon dioxide over the Amazon: New insights from stable isotopes, remote sensing and inverse modeling. [internal PhD, WU, Wageningen University]. Wageningen University. https://doi.org/10.18174/524771

Kuhn, M. A., Varner, R. K., Bastviken, D., Crill, P., MacIntyre, S., Turetsky, M., et al. (2021). BAWLD-CH₄: a comprehensive dataset of methane fluxes from boreal and arctic ecosystems. *Earth System Science Data*, *13*(11), 5151–5189. https://doi.org/10.5194/essd-13-5151-2021

Lacroix, F., Zaehle, S., Caldararu, S., Schaller, J., Stimmler, P., Holl, D., et al. (2022). Mismatch of N release from the permafrost and vegetative uptake opens pathways of increasing nitrous oxide emissions in the high Arctic. *Global Change Biology*, *28*(20), 5973–5990. https://doi.org/10.1111/gcb.16345

Lange, S. (2019). Trend-preserving bias adjustment and statistical downscaling with ISIMIP3BASD (v1.0). *Geoscientific Model Development*, *12*(7), 3055–3070. https://doi.org/10.5194/gmd-12-3055-2019

Lantuit, H., Overduin, P. P., Couture, N., Wetterich, S., Aré, F., Atkinson, D., et al. (2012). The Arctic Coastal Dynamics Database: A New Classification Scheme and Statistics on Arctic Permafrost Coastlines. *Estuaries and Coasts*, *35*(2), 383–400. https://doi.org/10.1007/s12237-010-9362-6

Lauerwald, R., Regnier, P., Figueiredo, V., Enrich-Prast, A., Bastviken, D., Lehner, B., et al. (2019). Natural Lakes Are a Minor Global Source of N_2O to the Atmosphere. *Global Biogeochemical Cycles*, *33*(12), 1564–1581. https://doi.org/10.1029/2019GB006261

Liu, S., Kuhn, C., Amatulli, G., Aho, K., Butman, D. E., Allen, G. H., et al. (2022). The importance of hydrology in routing terrestrial carbon to the atmosphere via global streams and rivers. *Proceedings of the National Academy of Sciences*, *119*(11), e2106322119. https://doi.org/10.1073/pnas.2106322119

Liu, Z., Kimball, J. S., Ballantyne, A. P., Parazoo, N. C., Wang, W. J., Bastos, A., et al. (2022). Respiratory loss during late-growing season determines the net carbon dioxide sink in

northern permafrost regions. *Nature Communications*, *13*(1), 5626. https://doi.org/10.1038/s41467-022-33293-x

López-Blanco, E., Exbrayat, J.-F., Lund, M., Christensen, T. R., Tamstorf, M. P., Slevin, D., et al. (2019). Evaluation of terrestrial pan-Arctic carbon cycling using a data-assimilation system. *Earth System Dynamics*, *10*(2), 233–255. https://doi.org/10.5194/esd-10-233-2019

López-Blanco, E., Langen, P. L., Williams, M., Christensen, J. H., Boberg, F., Langley, K., & Christensen, T. R. (2022). The future of tundra carbon storage in Greenland – Sensitivity to climate and plant trait changes. *Science of The Total Environment*, *846*, 157385. https://doi.org/10.1016/j.scitotenv.2022.157385

Lund, M., Raundrup, K., Westergaard-Nielsen, A., López-Blanco, E., Nymand, J., & Aastrup, P. (2017). Larval outbreaks in West Greenland: Instant and subsequent effects on tundra ecosystem productivity and CO2 exchange. *Ambio*, *46*(S1), 26–38. https://doi.org/10.1007/s13280-016-0863-9

Maavara, T., Lauerwald, R., Laruelle, G. G., Akbarzadeh, Z., Bouskill, N. J., Van Cappellen, P., & Regnier, P. (2019). Nitrous oxide emissions from inland waters: Are IPCC estimates too high? *Global Change Biology*, *25*(2), 473–488. https://doi.org/10.1111/gcb.14504

Marushchak, M. E., Kerttula, J., Diáková, K., Faguet, A., Gil, J., Grosse, G., et al. (2021). Thawing Yedoma permafrost is a neglected nitrous oxide source. *Nature Communications*, *12*(1), 7107. https://doi.org/10.1038/s41467-021-27386-2

Mauritsen, T., Bader, J., Becker, T., Behrens, J., Bittner, M., Brokopf, R., et al. (2019). Developments in the MPI-M Earth System Model version 1.2 (MPI-ESM1.2) and Its Response to Increasing CO_2. *Journal of Advances in Modeling Earth Systems*, *11*(4), 998–1038. https://doi.org/10.1029/2018MS001400

McGuire, A. D., Christensen, T. R., Hayes, D., Heroult, A., Euskirchen, E., Kimball, J. S., et al. (2012). An assessment of the carbon balance of Arctic tundra: comparisons among observations, process models, and atmospheric inversions. *Biogeosciences*, *9*(8), 3185–3204. https://doi.org/10.5194/bg-9-3185-2012

McGuire, A. David, Lawrence, D. M., Koven, C., Clein, J. S., Burke, E., Chen, G., et al. (2018). Dependence of the evolution of carbon dynamics in the northern permafrost region on the trajectory of climate change. *Proceedings of the National Academy of Sciences*, *115*(15), 3882–3887. https://doi.org/10.1073/pnas.1719903115

McGuire, D. A., Lawrence, D. M., Koven, C. D., Clein, J. S., Burke, E., Chen, G. S., et al. (2022). Projections of Permafrost Thaw and Carbon Release for RCP 4.5 and 8.5, 1901-2299. ORNL Distributed Active Archive Center. https://doi.org/10.3334/ORNLDAAC/1872

Mishra, U., Hugelius, G., Shelef, E., Yang, Y., Strauss, J., Lupachev, A., et al. (2021). Spatial heterogeneity and environmental predictors of permafrost region soil organic carbon stocks. *Science Advances*, *7*(9), eaaz5236. https://doi.org/10.1126/sciadv.aaz5236

Mörner, N.-A., & Etiope, G. (2002). Carbon degassing from the lithosphere. *Global and Planetary Change*, *33*(1–2), 185–203. https://doi.org/10.1016/S0921-8181(02)00070-X

Natali, S. M., Schuur, E. A. G., Mauritz, M., Schade, J. D., Celis, G., Crummer, K. G., et al. (2015). Permafrost thaw and soil moisture driving CO_2 and CH_4 release from upland tundra. *Journal of Geophysical Research: Biogeosciences*, *120*(3), 525–537. https://doi.org/10.1002/2014JG002872

Natali, S. M., Watts, J. D., Rogers, B. M., Potter, S., Ludwig, S. M., Selbmann, A.-K., et al. (2019). Large loss of CO2 in winter observed across the northern permafrost region. *Nature Climate Change*, *9*(11), 852–857. https://doi.org/10.1038/s41558-019-0592-8

Nitze, I., Grosse, G., Jones, B. M., Romanovsky, V. E., & Boike, J. (2018). Remote sensing quantifies widespread abundance of permafrost region disturbances across the Arctic and Subarctic. *Nature Communications*, *9*(1), 5423. https://doi.org/10.1038/s41467-018-07663-3

Obu, J. (2021). How Much of the Earth's Surface is Underlain by Permafrost? *Journal of Geophysical Research: Earth Surface*, *126*(5), e2021JF006123. https://doi.org/10.1029/2021JF006123

Obu, Jaroslav, Westermann, S., Bartsch, A., Berdnikov, N., Christiansen, H. H., Dashtseren, A., et al. (2019). Northern Hemisphere permafrost map based on TTOP modelling for 2000–2016 at 1 km2 scale. *Earth-Science Reviews*, *193*, 299–316. https://doi.org/10.1016/j.earscirev.2019.04.023

Olefeldt, D., Hovemyr, M., Kuhn, M. A., Bastviken, D., Bohn, T. J., Connolly, J., et al. (2021). The Boreal–Arctic Wetland and Lake Dataset (BAWLD). *Earth System Science Data*, *13*(11), 5127–5149. https://doi.org/10.5194/essd-13-5127-2021

Pallandt, M. M. T. A., Kumar, J., Mauritz, M., Schuur, E. A. G., Virkkala, A.-M., Celis, G., et al. (2022). Representativeness assessment of the pan-Arctic eddy covariance site network and optimized future enhancements. *Biogeosciences*, *19*(3), 559–583. https://doi.org/10.5194/bg-19-559-2022

Palmtag, J., Obu, J., Kuhry, P., Richter, A., Siewert, M. B., Weiss, N., et al. (2022). A high spatial resolution soil carbon and nitrogen dataset for the northern permafrost region based on circumpolar land cover upscaling. *Earth System Science Data*, *14*(9), 4095–4110. https://doi.org/10.5194/essd-14-4095-2022

Peylin, P., Law, R. M., Gurney, K. R., Chevallier, F., Jacobson, A. R., Maki, T., et al. (2013). *Global atmospheric carbon budget: results from an ensemble of atmospheric CO₂ inversions* (preprint). Biogeochemistry: Greenhouse Gases. https://doi.org/10.5194/bgd-10-5301-2013

Philip, S., Johnson, M. S., Baker, D. F., Basu, S., Tiwari, Y. K., Indira, N. K., et al. (2022). OCO-2 Satellite-Imposed Constraints on Terrestrial Biospheric CO_2 Fluxes Over South Asia. *Journal of Geophysical Research: Atmospheres*, *127*(3), e2021JD035035. https://doi.org/10.1029/2021JD035035

Potter, S., Cooperdock, S., Veraverbeke, S., Walker, X., Mack, M. C., Goetz, S. J., et al. (2023). Burned area and carbon emissions across northwestern boreal North America from 2001–2019. *Biogeosciences*, *20*(13), 2785–2804. https://doi.org/10.5194/bg-20-2785-2023

Qiu, C., Zhu, D., Ciais, P., Guenet, B., & Peng, S. (2020). The role of northern peatlands in the global carbon cycle for the 21st century. *Global Ecology and Biogeography*, *29*(5), 956–973. https://doi.org/10.1111/geb.13081

Qiu, H., Hao, D., Zeng, Y., Zhang, X., & Chen, M. (2023). Global and northern-high-latitude net ecosystem production in the 21st century from CMIP6 experiments. *Earth System Dynamics*, *14*(1), 1–16. https://doi.org/10.5194/esd-14-1-2023

Ramage J., et al., (in prep) The net GHG balance and budget of the permafrost region (2000-2020) from ecosystem flux upscaling. Companion paper to this manuscript, to be submitted to GBC in September 2023, draft included as supplement in this submission.

Rantanen, M., Karpechko, A. Yu., Lipponen, A., Nordling, K., Hyvärinen, O., Ruosteenoja, K., et al. (2022). The Arctic has warmed nearly four times faster than the globe since 1979. *Communications Earth & Environment*, *3*(1), 168. https://doi.org/10.1038/s43247-022-00498-3

Rodenhizer, H., Belshe, F., Celis, G., Ledman, J., Mauritz, M., Goetz, S., et al. (2022). Abrupt permafrost thaw accelerates carbon dioxide and methane release at a tussock tundra site. *Arctic, Antarctic, and Alpine Research*, *54*(1), 443–464. https://doi.org/10.1080/15230430.2022.2118639

Rößger, N., Wille, C., Veh, G., Boike, J., & Kutzbach, L. (2019). Scaling and balancing methane fluxes in a heterogeneous tundra ecosystem of the Lena River Delta. *Agricultural and Forest Meteorology*, *266–267*, 243–255. https://doi.org/10.1016/j.agrformet.2018.06.026

Rousk, K., Sorensen, P. L., & Michelsen, A. (2018). What drives biological nitrogen fixation in high arctic tundra: Moisture or temperature? *Ecosphere*, *9*(2), e02117. https://doi.org/10.1002/ecs2.2117

Runge, A., Nitze, I., & Grosse, G. (2022). Remote sensing annual dynamics of rapid permafrost thaw disturbances with LandTrendr. *Remote Sensing of Environment*, *268*, 112752. https://doi.org/10.1016/j.rse.2021.112752

Santoro, M.; Cartus, O. (2021): ESA Biomass Climate Change Initiative (Biomass_cci): Global datasets of forest above-ground biomass for the years 2010, 2017 and 2018, v2. Centre for Environmental Data Analysis, 17 March 2021. doi:10.5285/84403d09cef3485883158f4df2989b0c.

Saunois, M., Stavert, A. R., Poulter, B., Bousquet, P., Canadell, J. G., Jackson, R. B., et al. (2020). The Global Methane Budget 2000–2017. *Earth System Science Data*, *12*(3), 1561–1623. https://doi.org/10.5194/essd-12-1561-2020

Schuur, E. A. G., Abbott, B. W., Commane, R., Ernakovich, J., Euskirchen, E., Hugelius, G., et al. (2022). Permafrost and Climate Change: Carbon Cycle Feedbacks From the Warming Arctic. *Annual Review of Environment and Resources*, *47*(1), 343–371. https://doi.org/10.1146/annurev-environ-012220-011847

Sellar, A. A., Jones, C. G., Mulcahy, J. P., Tang, Y., Yool, A., Wiltshire, A., et al. (2019). UKESM1: Description and Evaluation of the U.K. Earth System Model. *Journal of Advances in Modeling Earth Systems*, *11*(12), 4513–4558. https://doi.org/10.1029/2019MS001739

Smallman, T. L., & Williams, M. (2019). Description and validation of an intermediate complexity model for ecosystem photosynthesis and evapotranspiration: ACM-GPP-ETv1. *Geoscientific Model Development*, *12*(6), 2227–2253. https://doi.org/10.5194/gmd-12-2227-2019

Smallman, T. L., Milodowski, D. T., Neto, E. S., Koren, G., Ometto, J., & Williams, M. (2021). *Parameter uncertainty dominates C cycle forecast errors over most of Brazil for the 21st Century* (preprint). Earth system interactions with the biosphere: biogeochemical cycles. https://doi.org/10.5194/esd-2021-17

Smith, S. L., O'Neill, H. B., Isaksen, K., Noetzli, J., & Romanovsky, V. E. (2022). The changing thermal state of permafrost. *Nature Reviews Earth & Environment*, *3*(1), 10–23. https://doi.org/10.1038/s43017-021-00240-1

Stanley, E. H., Casson, N. J., Christel, S. T., Crawford, J. T., Loken, L. C., & Oliver, S. K. (2016). The ecology of methane in streams and rivers: patterns, controls, and global significance. *Ecological Monographs*, *86*(2), 146–171. https://doi.org/10.1890/15-1027

Tarnocai, C., Canadell, J. G., Schuur, E. A. G., Kuhry, P., Mazhitova, G., & Zimov, S. (2009). Soil organic carbon pools in the northern circumpolar permafrost region: SOIL ORGANIC CARBON POOLS. *Global Biogeochemical Cycles*, *23*(2), n/a-n/a. https://doi.org/10.1029/2008GB003327

Taylor, K. E., Stouffer, R. J., & Meehl, G. A. (2012). An Overview of CMIP5 and the Experiment Design. *Bulletin of the American Meteorological Society*, *93*(4), 485–498. https://doi.org/10.1175/BAMS-D-11-00094.1

Terhaar, J., Lauerwald, R., Regnier, P., Gruber, N., & Bopp, L. (2021). Around one third of current Arctic Ocean primary production sustained by rivers and coastal erosion. *Nature Communications*, *12*(1), 169. https://doi.org/10.1038/s41467-020-20470-z

Tian, H., Xu, R., Canadell, J. G., Thompson, R. L., Winiwarter, W., Suntharalingam, P., et al. (2020). A comprehensive quantification of global nitrous oxide sources and sinks. *Nature*, *586*(7828), 248–256. https://doi.org/10.1038/s41586-020-2780-0

Treat, C. C., Bloom, A. A., & Marushchak, M. E. (2018). Nongrowing season methane emissions-a significant component of annual emissions across northern ecosystems. *Global Change Biology*, *24*(8), 3331–3343. https://doi.org/10.1111/gcb.14137

Treat, C. C., Marushchak, M. E., Voigt, C., Zhang, Y., Tan, Z., Zhuang, Q., et al. (2018). Tundra landscape heterogeneity, not interannual variability, controls the decadal regional carbon balance in the Western Russian Arctic. *Global Change Biology*, *24*(11), 5188–5204. https://doi.org/10.1111/gcb.14421

Treharne, R., Rogers, B. M., Gasser, T., MacDonald, E., & Natali, S. (2022). Identifying Barriers to Estimating Carbon Release From Interacting Feedbacks in a Warming Arctic. *Frontiers in Climate*, *3*, 716464. https://doi.org/10.3389/fclim.2021.716464

Turetsky, M. R., Abbott, B. W., Jones, M. C., Anthony, K. W., Olefeldt, D., Schuur, E. A. G., et al. (2020). Carbon release through abrupt permafrost thaw. *Nature Geoscience*, *13*(2), 138–143. https://doi.org/10.1038/s41561-019-0526-0

Van Den Hurk, B., Kim, H., Krinner, G., Seneviratne, S. I., Derksen, C., Oki, T., et al. (2016). LS3MIP (v1.0) contribution to CMIP6: the Land Surface, Snow and Soilmoisture Model Intercomparison Project – aims, setup and expected outcome. *Geoscientific Model Development*, *9*(8), 2809–2832. https://doi.org/10.5194/gmd-9-2809-2016

Van Der Werf, G. R., Randerson, J. T., Giglio, L., Van Leeuwen, T. T., Chen, Y., Rogers, B. M., et al. (2017). Global fire emissions estimates during 1997–2016. *Earth System Science Data*, *9*(2), 697–720. https://doi.org/10.5194/essd-9-697-2017

Veraverbeke, S., Delcourt, C. J. F., Kukavskaya, E., Mack, M., Walker, X., Hessilt, T., et al. (2021). Direct and longer-term carbon emissions from arctic-boreal fires: A short review of recent advances. *Current Opinion in Environmental Science & Health*, *23*, 100277. https://doi.org/10.1016/j.coesh.2021.100277

Virkkala, A., Aalto, J., Rogers, B. M., Tagesson, T., Treat, C. C., Natali, S. M., et al. (2021). Statistical upscaling of ecosystem CO_2 fluxes across the terrestrial tundra and boreal domain: Regional patterns and uncertainties. *Global Change Biology*, *27*(17), 4040–4059. https://doi.org/10.1111/gcb.15659

Virkkala, A.-M., Virtanen, T., Lehtonen, A., Rinne, J., & Luoto, M. (2018). The current state of CO_2 flux chamber studies in the Arctic tundra: A review. *Progress in Physical Geography: Earth and Environment*, *42*(2), 162–184. https://doi.org/10.1177/0309133317745784

Virkkala, A.-M., Natali, S. M., Rogers, B. M., Watts, J. D., Savage, K., Connon, S. J., et al. (2022). The ABCflux database: Arctic–boreal CO_2 flux observations and ancillary information aggregated to monthly time steps across terrestrial ecosystems. *Earth System Science Data*, *14*(1), 179–208. https://doi.org/10.5194/essd-14-179-2022

Voigt, C., Lamprecht, R. E., Marushchak, M. E., Lind, S. E., Novakovskiy, A., Aurela, M., et al. (2017). Warming of subarctic tundra increases emissions of all three important greenhouse gases - carbon dioxide, methane, and nitrous oxide. *Global Change Biology*, *23*(8), 3121–3138. https://doi.org/10.1111/gcb.13563

1403 Voigt, C., Marushchak, M. E., Mastepanov, M., Lamprecht, R. E., Christensen, T. R., Dorodnikov,
1404 M., et al. (2019). Ecosystem carbon response of an Arctic peatland to simulated permafrost
1405 thaw. *Global Change Biology*, *25*(5), 1746–1764. https://doi.org/10.1111/gcb.14574
1406 Voigt, C., Marushchak, M. E., Abbott, B. W., Biasi, C., Elberling, B., Siciliano, S. D., et al. (2020).
1407 Nitrous oxide emissions from permafrost-affected soils. *Nature Reviews Earth &*
1408 *Environment*, *1*(8), 420–434. https://doi.org/10.1038/s43017-020-0063-9
1409 Walker, X. J., Rogers, B. M., Veraverbeke, S., Johnstone, J. F., Baltzer, J. L., Barrett, K., et al.
1410 (2020). Fuel availability not fire weather controls boreal wildfire severity and carbon
1411 emissions. *Nature Climate Change*, *10*(12), 1130–1136. https://doi.org/10.1038/s41558-020-
1412 00920-8
1413 Walker, Xanthe J., Baltzer, J. L., Cumming, S. G., Day, N. J., Ebert, C., Goetz, S., et al. (2019).
1414 Increasing wildfires threaten historic carbon sink of boreal forest soils. *Nature*, *572*(7770),
1415 520–523. https://doi.org/10.1038/s41586-019-1474-y
1416 Walter Anthony, K. M., Anthony, P., Grosse, G., & Chanton, J. (2012). Geologic methane seeps
1417 along boundaries of Arctic permafrost thaw and melting glaciers. *Nature Geoscience*, *5*(6),
1418 419–426. https://doi.org/10.1038/ngeo1480
1419 Wiltshire, A. J., Burke, E. J., Chadburn, S. E., Jones, C. D., Cox, P. M., Davies-Barnard, T., et al.
1420 (2021). JULES-CN: a coupled terrestrial carbon–nitrogen scheme (JULES vn5.1).
1421 *Geoscientific Model Development*, *14*(4), 2161–2186. https://doi.org/10.5194/gmd-14-2161-
1422 2021
1423 Yu, T., & Zhuang, Q. (2020). Modeling biological nitrogen fixation in global natural terrestrial
1424 ecosystems. *Biogeosciences*, *17*(13), 3643–3657. https://doi.org/10.5194/bg-17-3643-2020
1425 Yuan, Y., Zhuang, Q., Zhao, B., & Shurpali, N. (2023). *Nitrous oxide emissions from pan-Arctic*
1426 *terrestrial ecosystems: A process-based biogeochemistry model analysis from 1969 to 2019*
1427 (preprint). Biogeochemistry: Greenhouse Gases. https://doi.org/10.5194/egusphere-2023-
1428 1047
1429 Zhang, Z., Fluet-Chouinard, E., Jensen, K., McDonald, K., Hugelius, G., Gumbricht, T., et al. (2021).
1430 Development of the global dataset of Wetland Area and Dynamics for Methane Modeling
1431 (WAD2M). *Earth System Science Data*, *13*(5), 2001–2023. https://doi.org/10.5194/essd-13-
1432 2001-2021
1433 Zheng, B., Ciais, P., Chevallier, F., Yang, H., Canadell, J. G., Chen, Y., et al. (2023). Record-high CO_2
1434 emissions from boreal fires in 2021. *Science*, *379*(6635), 912–917.
1435 https://doi.org/10.1126/science.ade0805
1436 Zhu, Q., Riley, W. J., Tang, J., Collier, N., Hoffman, F. M., Yang, X., & Bisht, G. (2019).
1437 Representing Nitrogen, Phosphorus, and Carbon Interactions in the E3SM Land Model:
1438 Development and Global Benchmarking. *Journal of Advances in Modeling Earth Systems*,
1439 *11*(7), 2238–2258. https://doi.org/10.1029/2018MS001571

Supplementary text and figures

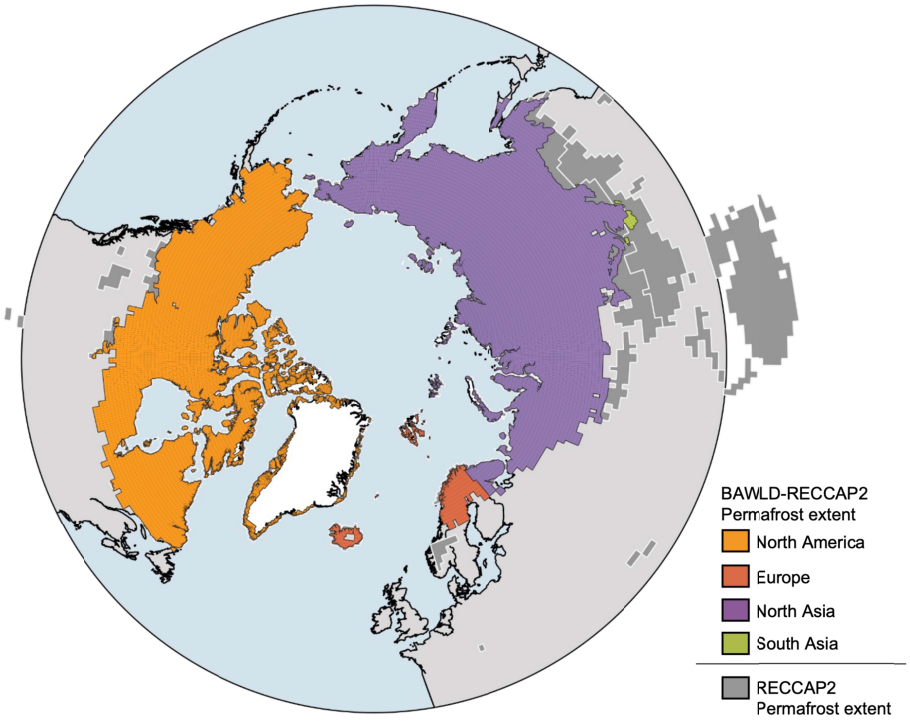

Figure S1. The spatial extent of permafrost defined in this study - the BAWLD-RECCAP2 permafrost region shown in relation other RECCAP2 regions as well as the full permafrost extent. The spatial extent of the permafrost region defined in this study as an overlap of the RECCAP2 permafrost extent and the Boreal Arctic Wetlands and Lakes Dataset (BAWLD, Olefeldt et al., 2021). The colours show regional overlap with different RECCAP2 regions (Ciais et al., 2022). The grey shades show the full

northern permafrost extent as defined by the combination of data from Obu et al. (2021) plus areas that recorded mean annual air temperature (MAAT) below 0°C between 1990 and 2000, which is consistent with the area used in the ISIMIP3 model intercomparison.

Detailed method description for CARDAMOM

The DALEC intermediate complexity model for terrestrial ecosystems simulates the C stocks, inputs (photosynthesis), outputs (respiration, fire and removals) and internal flows (allocation / turnover) of 4 biomass (labile, foliage, roots and wood) and two dead organic matter (litter and soil) pools (Bloom & Williams 2015; Smallman & Williams 2019). Photosynthesis is simulated by the ACM-GPP-ET model which estimates photosynthesis as a function of available CO_2, temperature, absorbed shortwave radiation, leaf area. Available CO_2 is a function of stomatal conductance which is itself determined by opening the stomatal until the additional photosynthate gained falls below a critical threshold or the limits of water supply from the soil via the roots is reached (for details see Smallman & Williams 2019). Photosynthate is allocated to autotrophic respiration and plant tissues based on fixed fractions. Allocation of labile to the canopy and canopy senescence are determined as a function of day of year. Turnover of wood and fine roots follows first order kinetics. Decomposition of litter to soil, and heterotrophic respiration from both litter and soil mineralisation follow first order kinetics modified by an exponential temperature response function. Each pool, and flux within DALEC and its exchanges with its environment are governed by parameters retrieved by CARDAMOM for each location independently, but as a function of local information.

CARDAMOM analysed terrestrial C-cycling at a monthly time step and 0.5 x 0.5 degree spatial resolution for 19 years (2001-2019). CARDAMOM combines information contained within the DALEC model structure, DALEC's drivers, the assimilated observations and ecological knowledge to estimate ensembles of local parameters. From these ensembles of parameters we can explicitly quantify at pixel scale uncertainty in both the underlying parameters and C-cycling. Meteorological drivers are drawn from the GSWP3-W5E5 dataset, fire is imposed as a function of MODIS burned area and forest loss is imposed using global forest watch (Hansen et al., 2013). Assimilated information are time series estimates of leaf area index (Copernicus Service Information 2021), woody biomass for 2017 and 2018 (Santoro et al., 2021), and net biome exchange of CO2 (Koren 2020). NCSCD provides pixel specific prior for the initial soil C content while a globally applied prior for the ratio of autotrophic respiration and photosynthesis (of 0.46 +/- 0.12, Collalti & Prentice 2019). Ecological knowledge is applied using ecological and dynamical constraints (EDCs) which ensure rejection of parameter combinations which are ecologically unrealistic, such as wood turnover being faster than fine root or inappropriate exponential changes in C stocks (for details see Bloom et al., 2016).

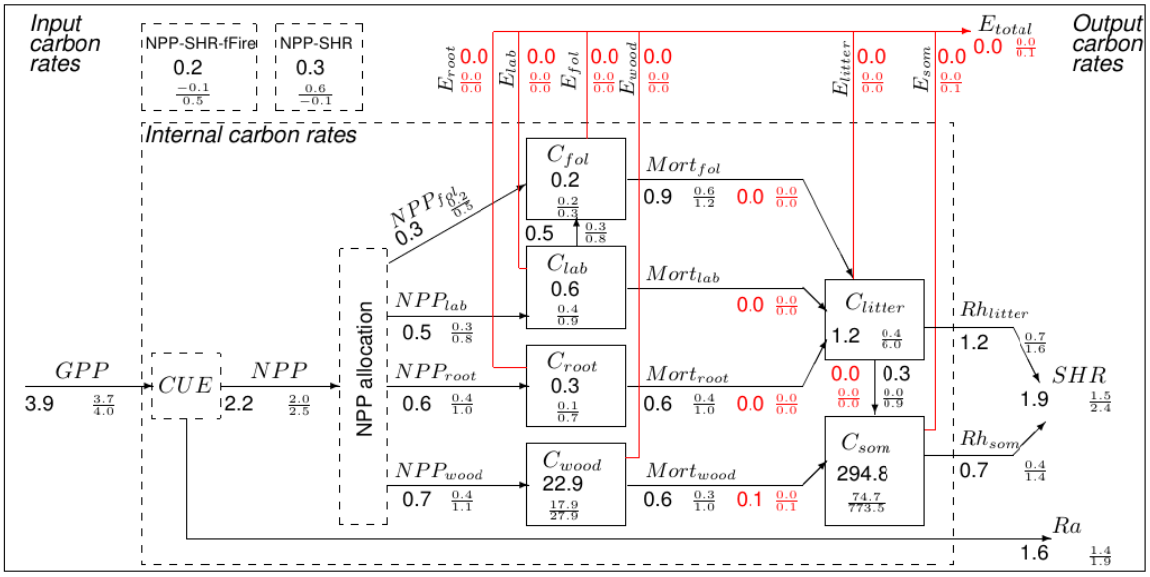

Figure S2: Steady state C-budget for RECCAP2-Permafrost. Numbers show median estimate of fluxes (alongside arrows) and of stocks (in boxes). Units are MgC ha-1 for stocks and MgC ha-1 yr-1 for fluxes. 95% confidence intervals are shown in a fractional form with 2.5 and 97.5 percentile as numerator and denominator. Black fluxes are biogenic, including net primary production (NPP), mortality (Mort), autotrophic respiration (Ra), and heterotrophic respiration (SHR). NEE = Ra + SHR - GPP. NBE = NEE + Etotal. Red fluxes are fire-driven emissions (E).

Process based model result separated to the Boreal and Tundra biomes

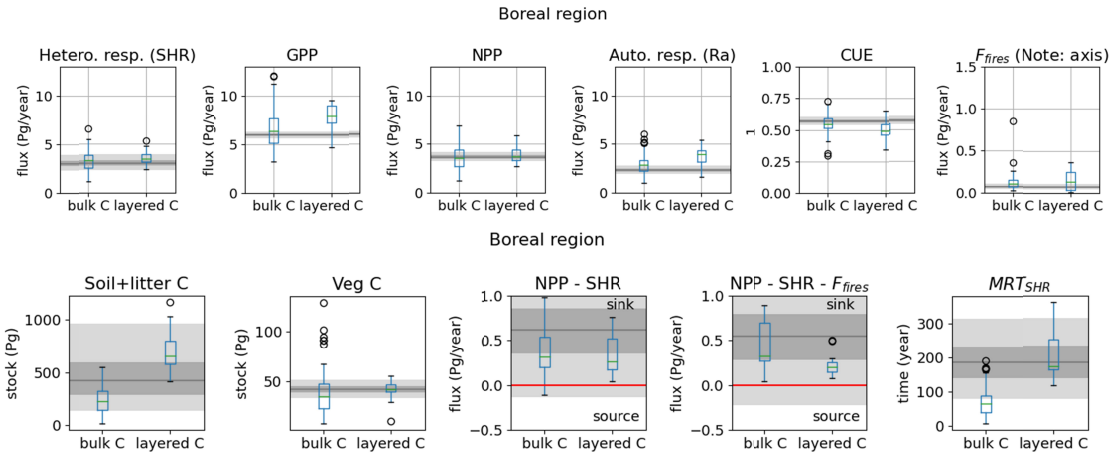

Figure S3.Carbon fluxes, stocks and relevant ecosystem properties from the process-based models listed in supplemental table S1 for the boreal region. The top row shows the following simulated multi-annual mean C fluxes (left to right) -

heterotrophic respiration (SHR); gross primary productivity (GPP); net primary productivity (NPP); autotrophic respiration (R_a) all in Pg CO_2-C y^{-1}. Also shown on the top row are the carbon use efficiency (CUE, dimensionless) and the fire C flux (F_{fires} in Pg CO_2-C y^{-1}). The bottom row shows C stocks (soil and litter carbon and vegetation carbon, both in Pg C), the net ecosystem productivity (NPP - SHR in Pg CO_2-C y^{-1}); and the net biome productivity (NPP - SHR - F_{fires} in Pg CO_2-C y^{-1}) for the models that include fire emissions. The final plot at the bottom right shows the mean residence time of dead organic matter (MRT_{SHR}; years). The model ensemble is divided into two sub ensembles depending on whether they have a representation of permafrost carbon. In each subplot the left hand box plot ("*bulk* C", n=55) represents models without permafrost carbon representation and the right hand box plot ("*layered* C", n=18) represents models which include permafrost carbon. The grey shading represents the likely range estimated by the observationally-informed CARDAMOM analysis. The solid grey line indicates the 50 % quantile, i.e. most likely estimate. The dark grey zone defines the 50 % confidence interval around the 50 % quantile while the light grey zone is the 95 % confidence interval also around the 50 % quantile. In the (NPP - SHR) and (NPP - SHR - F_{fires}) plots the red line is at zero and positive values are a net uptake of carbon.

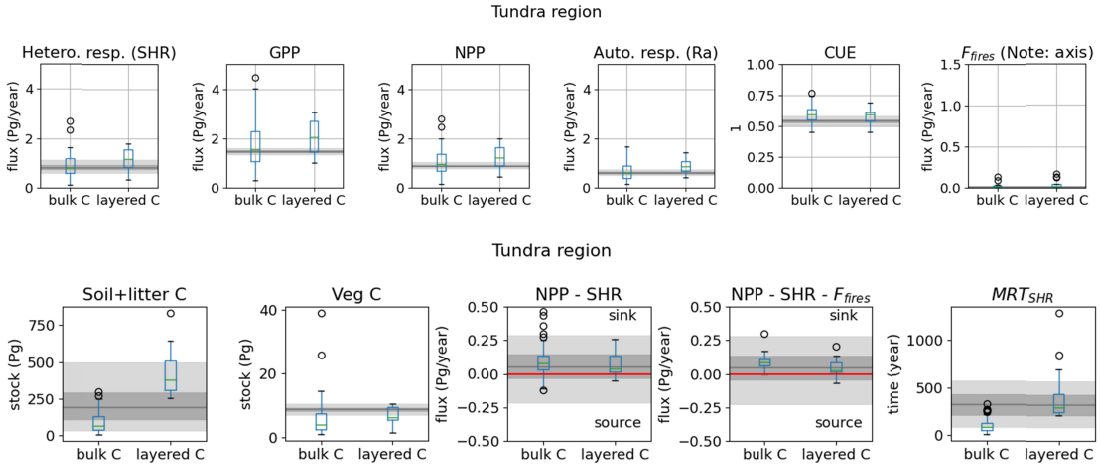

Figure S4. Carbon fluxes, stocks and relevant ecosystem properties from the process-based models listed in supplemental table S1 for the tundra region. The top row shows the following simulated multi-annual mean C fluxes (left to right) - heterotrophic respiration (SHR); gross primary productivity (GPP); net primary productivity (NPP); autotrophic respiration (R_a) all in Pg CO_2-C y^{-1}. Also shown on the top row are the carbon use efficiency (CUE, dimensionless) and the fire C flux (F_{fires} in Pg CO_2-C y^{-1}). The bottom row shows C stocks (soil and litter carbon and vegetation carbon, both in Pg C), the net ecosystem productivity (NPP - SHR in Pg CO_2-C y^{-1}); and the net biome productivity (NPP - SHR - F_{fires} in Pg CO_2-C y^{-1}) for the models that include fire emissions. The final plot at the bottom right shows the mean residence time of dead organic matter (MRT_{SHR}; years). The model ensemble is divided into two sub ensembles depending on whether they have a representation of permafrost carbon. In each subplot the left hand box plot ("*bulk* C", n=55) represents models without permafrost carbon representation and the right hand box plot ("*layered* C", n=18) represents models which include permafrost carbon. The grey shading represents the likely range estimated by the observationally-informed CARDAMOM analysis. The solid grey line indicates the 50 % quantile, i.e. most likely estimate. The dark grey zone defines the 50 % confidence interval around the 50 % quantile while the light grey zone is the 95 % confidence interval also around the 50 % quantile. In the (NPP - SHR) and (NPP - SHR - F_{fires}) plots the red line is at zero and positive values are a net uptake of carbon.

Table 1. Summary of annual budgets from process-based model ensembles and the model data-fusion approach CARDAMOM. For CO2 the mean from the full ensemble of models that include fire is presented as well as the annual budgets from CARDAMOM. For CH4 the annual fluxes from wetlands are reported. No process-based model results are available for N2O

Process-based models, annual budgets						
	CO2	**2.5% CI**	**97.5% CI**	**CH4**	**2.5% CI**	**97.5% CI**
	Tg CO2-C yr-1			**Tg CH4-C yr-1**		
Model ensemble: NPP- SHR - Ffire	**-340**	-930	90	*NA*		
Model ensemble: NPP - SHR	*-420*	*-1020*	*-80*			
Model ensemble: Ffire	120	10	460			
CARDAMOM: NPP- SHR - Ffire	**-870**	-1780	160	*NA*		
CARDAMOM: NPP - SHR	*-960*	-1880	20			
CARDAMOM: Ffire	*60*	50	100			
Model ensemble wetland CH4 flux	*NA*			**12**	8.6	16

Table 2. Summary of all main budget posts for the three GHGs from bottom-up ecosystem upscaling as presented by Ramage et al., (in prep).

Data-driven upscaling (All numbers from Ramage et al. in prep)										
	Surface area	**CO2**	**2.5% CI**	**97.5% CI**	**CH4**	**2.5% CI**	**97.5% CI**	**N2O**	**2.5% CI**	**97.5% CI**
	106 km2	**Tg CO2-C yr-1**			**Tg CH4-C yr-1**			**Tg N2O-N yr-1**		
Total budget	**17.05**	**0.4**	-620	652	**37.7**	21.3	52.8	**0.62**	0.03	1.19
Sum all terrestrial land cover:		*-340*	*-836*	*156*	*25.6*	*14.69*	*36.4*	*0.55*	*-0.03*	*1.14*
Sum uplands	*14.2*	*-267*	*-687*	*153*	*1*	*-2.6*	*4.5*	*0.37*	*0.03*	*0.72*
Boreal forests	*9*	*-270*	*-540*	*-1*	*-1.1*	*-2.2*	*0*	0.14	-0.01	0.3
Dry tundra	*5.2*	*2.9*	*-148*	*154*	*2.1*	*-0.4*	*4.5*	0.23	0.04	0.42
Sum wetlands	*2.8*	*-72*	*-148*	*4*	*24.6*	*17.29*	*31.9*	*0.18*	*-0.06*	*0.42*
Non-permafrost wetlands	*1.6*	*-69*	*-125*	*-14*	*21*	*14*	*27*	0.07	-0.03	0.17
Permafrost bogs	*0.86*	*-0.05*	*-0.8*	*0.73*	*0.7*	*0.29*	*1.1*	0.1	-0.03	0.23
Tundra wetlands	*0.4*	*-2.7*	*-23*	*17*	*3.3*	*2.7*	*3.9*	0.01	0	0.02
Fires	1.1	109	84	135	1.2	0.93	1.45	0.07	0.057	0.083
Inland waters	1.4	231	132	360	9.4	4.5	13.1	*0.002*	0.001	0.003
Geological emissions		*NA*	*NA*	*NA*	1.5	1.2	1.8	*NA*		

Table 3. Summary of the different budget components used to generate an integrated bottom-up budget for all three GHGs.

		CO2	2.5% CI	97.5% CI	CH4	2.5% CI	97.5% CI	N2O	2.5% CI	97.5% CI
		Tg CO2-C yr-1			Tg CH4-C yr-1			Tg N2O-N yr-1		
Data-driven synthesis	Total budget	0.4	-620	652	38	21	53	0.6	0.03	1.2
	Sum upland landcover types	*-267*	*-687*	*153*	*1*	*-2.6*	*4.5*	*0.37*	*0.03*	*0.72*
	Sum wetlands	*-72*	*-148*	*4*	*25*	*17*	*32*	*0.18*	*-0.06*	*0.42*
	Fires	*109*	*84*	*135*	*1.2*	*0.9*	*1.5*	*0.07*	*0.06*	*0.08*
	Inland waters	*231*	*132*	*360*	*9.4*	*4.5*	*13*	*0.002*	*0.001*	*0.003*
Abrupt thaw wetland flux	*(not included in data-driven upscaling total)*	*19*	*13*	*26*	*19*	*12*	*26*			
Process-based models	Model ensemble NEE (NPP- SHR - Ffire)	-340	-930	90	*NA*			*NA*		
	Model ensemble CH4 wetland flux	*NA*			12	8.6	16	*NA*		
Integrated bottom-up budget	**Natural ecosystems (including fires)**	**-31**	**-667**	**559**	**38**	23	53	**0.6**	0.03	1.2
	Mean vegetated upland+wetland ecosystems (with fire)	-262	-799	200	29	18	40	*NA*		
	Data-driven, sum upland+wetland landcover types	-230	-757	292	27	15.6	37.9	0.6	0	1.2
	Model ensemble NEE plus and wetland abrupt thaw	-293	-842	109	*NA*			*NA*		
	Model ensemble wetland CH4 flux and abrupt wetland thaw				31	21	42			
	Inland waters (from data-driven synthesis)	231	132	360	9.4	4.5	13	0.002	0.001	0.003

Table 4: Summary table of GHG emissions (annual mean and 95% CI) from the RECCAP2 permafrost domain from atmospheric inversion models. The reported inverse model fluxes are the ecosystem fluxes, not including anthropogenic emissions. Sub-fluxes from fires (already included in the total) are also shown for CO2 and CH4.

	CO2			CH4			N2O		
	Tg CO2-C yr-1	2.5% CI	97.5% CI	Tg CH4-C yr-1	2.5% CI	97.5% CI	Tg N2O-N yr-1	2.5% CI	97.5% CI
Inversion ensemble 2000-2009*	-526	-802	-250	14	11	18	0.01	-0.24	0.27
*Fire sub-flux***	*72.8*	*48.048*	*97.552*	*1.235*	*1*	*1.47*	*NA*		
Inversion ensemble 2010-2020*	-643	-917	-369	15	12	18	0.16	-0.14	0.46
*Fire sub-flux***	*82.1*	*54.186*	*110.014*	*1.6*	*1.4*	*1.7*	*NA*		
Inversion ensemble 2000-2020*	-587	-862	-312	15	11	18	0.09	-0.19	0.37
*Fire sub-flux***	*77.7*	*51.282*	*104.118*	*1.4*	*1.2*	*1.6*	*NA*		

* GHG are reported for different periods: 2000-2020 for CO2, 2000-2017 for CH4, and 2000-2019 for N2O

**Fire sub-flux of CO2 from Zheng et al., (2023) CI range assumed to be proportional to reported CI for trends in that paper. Fire sub-flux of CH4 is biomass and biofuel burning extracted by mask from global methane budget datasets used in Saunois et al (2020).

Table 5. Summary of all main budget posts for the three GHGs, including anthropogenic fluxes as well as lateral fluxes and total sum changes of C and N.

		CO2	2.5% CI	97.5% CI	CH4	2.5% C	97.5% CI	N2O	2.5% CI	97.5% CI
		Tg CO2-C yr-1			Tg CH4-C yr-1			Tg N2O-N yr-1		
Bottom-up integrated budget	All ecosystems (including fires)	-31	-667	559	38	23	53	0.6	0.03	1.2
Top-down atmosperic inversions	All ecosystems (including fires)	-587	-862	-312	15	11	18	0.09	-0.19	0.37
Anthropogenic emissions	Total budget	73	56	89	5.4	3.8	7.1	*NA*		
	Fossil fuels	*73*	*56*	*89*	*4.9*	*3.3*	*6.5*	*NA*		
	Agriculture and waste	*NA*			*0.54*	*0.44*	*0.64*	*NA*		
		Carbon stock changes						Nitrogen stock changes		
		Tg C yr-1	2.5% CI	97.5% CI				Tg N yr-1	2.5% CI	97.5% CI
Mean gas C (CO2+CH4) and N (N2O) budget	Bottom-up	7	-644	612				0.6	0.03	1.2
	Top-down	-573	-851	-294				0.09	-0.19	0.37
Lateral flux C and N budgets		94	79	111				2.6	1.9	3.6
	Riverine flux	*78*	*70*	*87*				*1.0*	*0.9*	*1.1*
	Coastal erosion	*15*	*9.2*	*24*				*1.6*	*1.0*	*2.5*
Sum C and N changes	Bottom-up	101	-565	723				3.2	1.93	4.8
	Top-down	-479	-772	-183				2.7	1.7	4.0
	Mean bottom-up/top-down	-189	-669	270				2.9	1.8	4.4

Table 6. Summary of annual GHGs budgets for all main budget posts, converted to CO2-equivalents (Tg CO2-Ceq, with 95% CI) using a 100-year Global Warming Potential (GWP-100) from bottom-up approaches, top-down atmospheric inversion models and from anthropogenic fluxes. A GWP-100 of 29.8 for CH4 and 273 or N2O relative to CO2 was used (IPCC, 2023; Table 7.15).

	GWP100	CO2	2.5% CI	97.5% CI	CH4	2.5% CI	97.5% CI	N2O	2.5% CI	97.5% CI	Total GHGs	2.5% CI	97.5% CI
		Tg CO2-Ce yr-1			Tg CO2-Ce yr-1			Tg CO2-Ce yr-1			Tg CO2eq yr-1		
Integrated bottom-up budge	Natural ecosystems (including fires)	-31	-667	559	410	248	572	70	3.5	140	449	-415	1272
	Mean vegetated upland+wetland ecosyste	*-262*	*-799*	*200*	*313*	*194*	*432*	*NA*			*52*	*-605*	*632*
	Data-driven, sum upland+wetland landcov	*-230*	*-757*	*292*	*292*	*168*	*409*	*70*	*0*	*140*	*132*	*-588*	*841*
	Model NEE and wetland abrupt thaw	*-293*	*-842*	*109*	*NA*			*NA*			*-293*	*-842*	*109*
	Model wetland CH4 flux and abrupt wetland thaw				*335*	*227*	*454*				*335*	*227*	*454*
	Inland waters (from data-driven synthesis)	*230*	*132*	*359*	*102*	*49*	*140*	*0.23*	*0.12*	*0.35*	*332*	*181*	*500*
	Fires (from data-driven synthesis)	*109*	*80*	*136*	*13*	*10*	*16*	*8.2*	*7.0*	*9.3*	*130*	*97*	*162*
Top-down atmospheric inver	Natural ecosystems (including fires)	-587	-862	-312	162	119	194	11	-22	43	-414	-765	-74
	Fires (from one inversion system)	*78*	*51*	*104*	*NA*			*NA*			*78*	*51*	*104*
Anthropogenic fluxes	Fossil fuel, agriculture and waste, cement	73	56	89	57	41	72				129	98	161
Summary of all fluxes	Bottom-up plus anthropogenic	41	-611	648	467	290	644	70	3.5	140	579	-317	1432
	Top-down plus anthropogenic	-514	-806	-223	219	160	266	11	-22	43	-285	-668	86
	Mean bottom-up/top-down plus anthropogenic	-237	-708	212	343	225	455	40	-9.3	92	147	-492	759